Journal of *Marine Science and Engineering*

MDPI

Article

Prediction of the Propeller Performance at Different Reynolds Number Regimes with RANS

João Baltazar [1,*], Douwe Rijpkema [2] and José Falcão de Campos [1]

[1] MARETEC—Marine, Environment and Technology Centre, LARSyS, Instituto Superior Técnico, Universidade de Lisboa, Av. Rovisco Pais 1, 1049-001 Lisboa, Portugal; falcao.campos@tecnico.ulisboa.pt
[2] MARIN—Maritime Research Institute Netherlands, 2 Haagsteeg, 6708 PM Wageningen, The Netherlands; d.r.rijpkema@marin.nl
* Correspondence: joao.baltazar@tecnico.ulisboa.pt; Tel.: +351-218-419-289

Abstract: In this study, a Reynolds averaged Navier-Stokes solver is used for prediction of the propeller performance in open-water conditions at different Reynolds numbers ranging from 10^4 to 10^7. The $k-\omega$ SST turbulence model and the $\gamma - \tilde{\mathrm{Re}}_{\theta_t}$ correlation-based transition model are utilised and results compared for a conventional marine propeller. First, the selection of the turbulence inlet quantities for different flow regimes is discussed. Then, an analysis of the iterative and discretisation errors is made. This work is followed by an investigation of the predicted propeller flow at variable Reynolds numbers. Finally, the propeller scale-effects and the influence of the turbulence and transition models on the performance prediction are discussed. The variation of the flow regime showed an increase in thrust and decrease in torque for increasing Reynolds number. From the comparison between the turbulence model and the transition model, different flow solutions are obtained for the Reynolds numbers between 10^5 and 10^6, affecting the scale-effects prediction.

Keywords: marine propeller; flow regimes; RANS equations; turbulence and transition models; scale effects

Citation: Baltazar, J.; Rijpkema, D.; Falcão de Campos, J. Prediction of the Propeller Performance at Different Reynolds Number Regimes with RANS. *J. Mar. Sci. Eng.* **2021**, *9*, 1115. https://doi.org/10.3390/jmse9101115

Academic Editor: Alon Gany

Received: 14 September 2021
Accepted: 7 October 2021
Published: 14 October 2021

1. Introduction

The prediction of propeller performance in full-scale is usually based on model-scale experiments carried out in a towing tank or cavitation tunnel. Then, the full-scale performance is subsequently determined using simple extrapolation procedures from the model-scale results. One of the most widely used scaling approaches is the 1978 ITTC (International Towing Tank Conference) performance prediction method [1]. In the ITTC method the model-scale thrust and torque coefficients are corrected to the full-scale from the estimated change in drag coefficient at a representative blade section, usually at 0.75 of the propeller radius. These corrections are also function of the number of blades, blade pitch ratio, and chord length and thickness at the representative blade section. The corrections include also the effect of surface roughness on the section drag of the full-scale propeller. In the ITTC method only the effect of Reynolds number on the drag coefficient is taken into account. In addition, two propellers with different skew and rake distributions will give similar corrections.

Although the ITTC method is able to provide acceptable corrections for typical propulsive systems, its application to new propulsive configurations like high skewed propellers, ducted propellers, energy saving devices or tip loaded propellers may not reflect correctly the effect of the Reynolds number on the propeller characteristics due to the change in the flow regime. The flow around marine propellers in full-scale is assumed to be fully-turbulent. However, at model-scale different flow patterns may occur simultaneously: laminar flow, transition to turbulent, and turbulent flow. Additionally, flow separation may occur at model-scale, which is not present at full-scale. In this sense, the 27th and

28th ITTC [2,3] encourage the examination of the existence procedures and the use of CFD (Computational Fluid Dynamics) to clarify the scaling problems.

The blade boundary-layer regime may be obtained from the direction of the paint streaks. Surface flow patterns from paint-tests have been investigated by Meyne [4] and Kuiper [5,6] and have been related to laminar and turbulent boundary layer development on propeller blades. If the boundary-layer is laminar, the paint streaks are more radially directed due to the dominance of the centrifugal forces. Instead, if the boundary layer is turbulent, the paint streaks are more chordwise directed due the higher shear forces. A discussion on the different boundary-layer regimes that may be found on a marine propeller is given in Kuiper [6]. Alternatively, skin friction measurement techniques may be used not only to detect the boundary layer transition and quantify the skin friction distribution, but also to identify flow details, like flow patterns and separation bubbles. These techniques are being mainly used in the aerodynamic analysis of aircraft propellers and there is an extensive literature on this field. For early reviews of these techniques we refer to [7,8]. Recently, Wolf et al. [9] presented a review on the different techniques applied to transition measurements. However, these techniques have not been used in boundary layer measurements of marine propellers and ships.

Complementary to model tests, due to the advances in high-performance computing Reynolds-averaged Navier-Stokes (RANS) solvers are increasingly being used for the prediction of the propeller performance and quantification of the scale-effects. One of the pioneering efforts to investigate propeller scale effects using a RANS approach is attributed to Stanier [10], who calculated the flow in model- and full-scale using a fully turbulent model. Similar studies using a RANS method complemented with turbulence models, that were developed for fully turbulent flows, have been carried out for the analysis of the scale effect on marine propellers [11–14]. In these studies, from the analysis of the blade boundary-layer flow a more circumferentially directed flow is obtained with respect to paint tests, indicating an over-prediction of the turbulent boundary-layer. A large variety of studies have been also presented for ducted propellers. Abdel-Maksoud and Heinke [15], Haimov et al. [16], Rijpkema and Vaz [17], among others, analysed the influence of the Reynolds number on the propeller performance. The results showed that the calculated flows agree well with the observed trends at full-scale. However, since laminar-turbulent flow transition was not taken into account, reliable scale-effects may not be achieved.

Therefore, the use of turbulence models able to deal with laminar-to-turbulent transition is crucial. Several models have been proposed in the literature to simulate transitional flows with RANS and their application to marine propellers is growing. The most common models for application to marine propellers are the $\gamma - \tilde{\mathrm{Re}}_{\theta_t}$ correlation-based transition model [18,19], which solves transport equations for the intermittency factor that changes from zero (fully laminar flow) to one (fully turbulent flow) in the transition region and the momentum thickness Reynolds number Re_θ, and the $k_T - k_L - \omega$ model of Walters and Cokljat [20], based on the concept of laminar kinetic energy.

The first calculations using the $\gamma - \tilde{\mathrm{Re}}_{\theta_t}$ correlation-based transition model to marine propellers were presented by Müller [21]. In subsequent studies [22], the influence of Reynolds number and inlet turbulence intensity on the transition location predicted by the $\gamma - \tilde{\mathrm{Re}}_{\theta_t}$ correlation-based transition model was investigated. Results showed that the specification of reference values for the turbulence quantities at the inlet and the control of turbulence decay to the vicinity of the propeller is not straightforward. Yao and Zhang [23] proposed a simple method to estimate the transition position only based on the propeller geometry and advance coefficient. In a different way, Baltazar et al. [24] selected the inlet turbulence quantities to give the best qualitative agreement in comparison with the paint-tests. Alternatively, Gaggero [25] fixed the inlet turbulence quantities to obtain a turbulence intensity close to 1% at the propeller plane. In both cases [24,25], large and non-realistic values of the turbulence intensity and eddy-viscosity ratio were specified at the inlet. The influence of transition modelling on the propeller characteristics has been investigated using the $\gamma - \tilde{\mathrm{Re}}_{\theta_t}$ correlation-based transition model on a large

variety of cases. [26,27] applied the model to ducted propellers. Krasilnikov et al. [28] analysed the scale effects on the performance characteristics of twin-screw offshore vessels, and Moran-Guerrero et al. [29] investigated the influence of the cross-flow effects on the open-water predictions.

More recently, the prediction of laminar-to-turbulent flow transition on model-scale propeller has been extended to cavitating conditions. Viitanen [30] combined RANS turbulence modelling approaches with a mass-transfer model to study single and two-phase flows at different Reynolds number regimes. Transition was accounted by using the $\gamma - \tilde{\mathrm{Re}}_{\theta_t}$ correlation-based transition model for the model-scale simulations. Similar results between the different turbulence models at model-scale were obtained for both propeller forces and cavitation patterns. The comparison between the model- and full-scale indicated a slight increase in thrust and a lower torque in full-scale conditions at both wetted and cavitating cases. In Gaggero [31] the $\gamma - \tilde{\mathrm{Re}}_{\theta_t}$ correlation-based transition model and a modified mass transfer model based on the Schnerr-Sauer formulation have been used to account for the effect that the laminar boundary-layer has on cavitation inception. The numerical results showed a improvement in the agreement with the observations, when compared to the original Schnerr-Sauer cavitation model [32].

In addition, the prediction of the propeller performance at model-scale using the $k_T - k_L - \omega$ model has been investigated. This model solves the transport equations for the turbulent kinetic energy (k_T), laminar kinetic energy (k_L) and specific dissipation rate (ω). Wang and Walters [33] and Gaggero and Villa [34] compared the numerical results of the $k_T - k_L - \omega$ model with fully turbulent models and experimental measurements. From the comparisons, an improvement in the propeller performance prediction with the transition-sensitive model is obtained. However, the model seems to be less prone to transition, since from the analysis of the orientation of the streamlines, the flow is mainly laminar. Furthermore and similarly to what has been identified with the $\gamma - \tilde{\mathrm{Re}}_{\theta_t}$ correlation-based transition model, based on studies carried out for a flat plate [35], a strong dependence on the inlet turbulence quantities to the location of the transition region is observed.

For the prediction of scale-effects with RANS, the most common choice for turbulence modelling has been the Shear-Stress Transport (SST) two-equation linear eddy-viscosity model [36,37]. It is known that this turbulence model predicts well the viscous flow for fully developed turbulent flows, but it is not able to model the transition from laminar to turbulent flow. Eça and Hoekstra [38] tested, for the case of a flat plate, several turbulence models including the $k - \omega$ two-equation model proposed by Wilcox [39] and its SST variant. Results showed that transition occurs at a too low Reynolds number, and only a small region of laminar flow is obtained at the leading edge of the plate.

In order to take into account the effect of flow transition at model-scale in the computation of the scale-effects, the selection of a turbulence-transition model is crucial for the prediction of the propeller performance. In Baltazar et al. [24], simulations obtained with the $k - \omega$ SST turbulence model [37] and $\gamma - \tilde{\mathrm{Re}}_{\theta_t}$ correlation-based transition model [19] were compared to experimental paint-tests carried out at model-scale for two marine propellers. Additionally, a similar study was carried out for a third marine propeller for which three-dimensional velocity component measurements on the blade boundary-layer are available at model-scale [40]. In this case the comparison between the experimental data and the numerical results comprehended the blade pressure distributions, chordwise and radial components of the boundary-layer velocity profiles and boundary-layer characteristics. From these studies, an improvement in the flow pattern was achieved with the $\gamma - \tilde{\mathrm{Re}}_{\theta_t}$ transition model, which however, are highly dependent on the selected turbulence inlet quantities and limits its predictive capabilities.

As a continuation to the previous work [24,40], where a good agreement was obtained not only for the limiting streamlines, but also from the comparison of velocity profile measurements on smooth and tripped blades and boundary layer characteristics at model-scale, the $\gamma - \tilde{\mathrm{Re}}_{\theta_t}$ correlation-based transition model proposed by Langtry and Menter [19] is extended for the prediction of the viscous flow at a wide range of Reynolds numbers.

To understand the importance of transition modelling in the prediction of the scale-effects, results are compared with the $k-\omega$ SST turbulence model predictions [37]. In the literature, the $\gamma-\tilde{\mathrm{Re}}_{\theta_t}$ transition model is used for the predictions at model-scale and the $k-\omega$ SST turbulence model at full-scale. In this study, both models are analysed ranging from a low Reynolds number to a full-scale condition to understand their differences and limitations in the prediction of the propeller performance. However, due to the limitations of the $\gamma-\tilde{\mathrm{Re}}_{\theta_t}$ transition model for blind predictions of the propeller flow, the selection of the inlet turbulence quantities for the different Reynolds numbers is discussed in detail. This study includes also an estimation of the iterative and discretisation errors for three Reynolds numbers. The analysis of the predicted propeller flows at the different Reynolds numbers include the limiting streamlines on the blade surfaces, blade pressure and skin friction distributions and boundary-layer characteristics. In this paper, viscous flow calculations using a RANS method are presented for a marine propeller in open-water conditions at different Reynolds numbers ranging from 10^4 to 10^7. From the analysis of the propulsive predictions, an estimation of the scale-effect between full-scale and model-scale is presented. The paper is organised as follows: the mathematical model including the turbulence and transition models are given in Section 2; the propeller geometry, flow solver, and numerical set-up are described in Section 3; results are presented and discussed in Section 4; the paper ends with the main conclusions of this study.

2. Mathematical Model

2.1. RANS Equations

The flow simulation is based on the solution of the RANS equations. We introduce two reference frames: an inertial earth-fixed reference frame (X, Y, Z) or X_i with $(i = 1, 2, 3)$, and a non-inertial propeller-fixed reference frame (x, y, z) or x_i, which is rotating with constant angular velocity Ω. The mean velocity vector defined in respect to the earth-fixed reference frame (the so-called absolute velocity) is given by U_i, and defined in respect to the propeller-fixed reference, also known as the relative velocity, is given by V_i. If we consider that the propeller is operating in open-water conditions, then the flow is statistically steady in the propeller-fixed reference frame.

Assuming that the fluid is incompressible, the RANS (continuity and momentum) equations written in the propeller-fixed reference frame x_i and considering as the unknown the mean velocity in respect to the earth-fixed reference frame U_i, take the form

$$\begin{aligned} &\frac{\partial U_i}{\partial x_i} = 0, \\ &\rho\frac{\partial (V_j U_i)}{\partial x_j} + \rho\varepsilon_{ijk}\Omega_j U_k = -\frac{\partial P}{\partial x_i} + \frac{\partial}{\partial x_j}\left[(\mu+\mu_t)\left(\frac{\partial U_i}{\partial x_j}+\frac{\partial U_j}{\partial x_i}\right)\right], \end{aligned} \tag{1}$$

where ρ is the fluid density, μ the fluid viscosity, μ_t the eddy-viscosity and ε the Levi-Civita symbol. The modified pressure is given by $P = p + 2/3\rho k$, where p is the static pressure with the hydrostatic pressure as the reference, and k the turbulence kinetic energy. In this work, the Reynolds stresses are determined from the turbulence and transition models, which are based on the Boussinesq eddy-viscosity hypothesis [41]. We note that in this formulation, the Coriolis and centripetal accelerations are simplified into a single term $\varepsilon_{ijk}\Omega_j U_k$, which reduces the number of source terms of the momentum equation.

2.2. $k-\omega$ SST Turbulence Model

The SST two-equation turbulence model proposed by Menter et al. [37] is selected to solve the transport equations for the turbulence kinetic energy k:

$$\rho\frac{\partial (V_j k)}{\partial x_j} = P_k - \beta^*\rho\omega k + \frac{\partial}{\partial x_j}\left(\mu_k\frac{\partial k}{\partial x_j}\right), \tag{2}$$

and for the turbulence dissipation rate ω:

$$\rho\frac{\partial(V_j\omega)}{\partial x_j} = P_\omega - \beta\rho\omega^2 + \frac{\partial}{\partial x_j}\left(\mu_\omega\frac{\partial\omega}{\partial x_j}\right) + \frac{\sigma_d}{\omega}\frac{\partial k}{\partial x_j}\frac{\partial\omega}{\partial x_j}, \tag{3}$$

where P_k and P_ω are the production terms of the turbulence kinetic energy and turbulence dissipation rate, respectively. $D_k = \beta^*\rho\omega k$ and $D_\omega = \beta\rho\omega^2$ are the destruction terms of the turbulence kinetic energy and turbulence dissipation rate, respectively. The SST formulation is a combination of two of the most commonly-used two-equation models. The $k-\omega$ model [39] is used in the sub- and log-layer and gradually switches to the $k-\epsilon$ model [42] in the wake region of the boundary-layer and in free shear flows. The blending between the two models is made via the F_1 function. In this model, the coefficients are:

$$\begin{aligned}
&\beta^* = 0.09,\\
&\beta = 0.0828 - 0.0078F_1,\\
&\mu_k = \mu + (1 - 0.15F_1)\mu_t,\\
&\mu_\omega = \mu + (0.856 - 0.356F_1)\mu_t,\\
&\sigma_d = 1.712(1 - F_1)\rho.
\end{aligned} \tag{4}$$

The eddy-viscosity μ_t is defined as follows:

$$\mu_t = \frac{\rho a_1 k}{\max(a_1\omega, S\,F_2)}, \tag{5}$$

where S is the strain rate magnitude, F_2 a second blending function and $a_1 = 0.31$. The definitions of the blending functions F_1 and F_2 may be found in Menter et al. [37].

2.3. $\gamma - \tilde{\mathrm{Re}}_{\theta_t}$ Correlation-Based Transition Model

In this work, the $\gamma - \tilde{\mathrm{Re}}_{\theta_t}$ correlation-based transition model proposed by Langtry and Menter [19] is selected for transition prediction. This transition model contains two transport equations and accounts for transition due to free-stream turbulence intensity, pressure gradients and separation. One is a transport equation for intermittency γ:

$$\rho\frac{\partial(V_j\gamma)}{\partial x_j} = P_\gamma - E_\gamma + \frac{\partial}{\partial x_j}\left[\left(\mu + \frac{\mu_t}{\sigma_f}\right)\frac{\partial\gamma}{\partial x_j}\right], \tag{6}$$

where P_γ and E_γ are the production and relaminarisation terms, respectively. The second one is a transport equation for the local transition onset momentum thickness Reynolds number $\tilde{\mathrm{Re}}_{\theta_t}$:

$$\rho\frac{\partial(V_j\tilde{\mathrm{Re}}_{\theta_t})}{\partial x_j} = P_{\theta t} + \frac{\partial}{\partial x_j}\left[\sigma_{\theta t}(\mu + \mu_t)\frac{\partial\tilde{\mathrm{Re}}_{\theta_t}}{\partial x_j}\right], \tag{7}$$

which only includes a production term $P_{\theta t}$. The terms P_γ, E_γ and $P_{\theta t}$ and the constants σ_f and $\sigma_{\theta t}$ are given in [19].

This model is also sometimes known as the $\gamma - \tilde{\mathrm{Re}}_{\theta_t} -$ SST model, because it makes use of the equations for γ and $\tilde{\mathrm{Re}}_{\theta_t}$, in addition to the k and ω equations of the SST turbulence model [37]. Therefore, this model corresponds to a four-equation transition SST turbulence model. We note that the definitions of production and dissipation terms of the k-equation, and the blending function F_1 change due to the coupling with the $\gamma - \tilde{\mathrm{Re}}_{\theta_t}$ transition model. The equation for ω is not changed. Therefore, P_k, D_k and F_1 are replaced by $\tilde{P}_k$, $\tilde{D}_k$ and $\tilde{F}_1$, defined as

$$\begin{aligned}
\tilde{P}_k &= \gamma_{\text{eff}} P_k, \\
\tilde{D}_k &= \min(\max(\gamma_{\text{eff}}, 0.1), 1.0) D_k, \\
\tilde{F}_1 &= \max(F_1, F_3), \\
F_3 &= \exp\left[-\left(\frac{R_y}{120}\right)^8\right], \\
R_y &= \frac{\rho d \sqrt{k}}{\mu},
\end{aligned} \tag{8}$$

where d is the wall distance and γ_{eff} is defined by

$$\gamma_{\text{eff}} = \max(\gamma, \gamma_{\text{sep}}), \tag{9}$$

where γ_{sep} is related to separation-induced transition.

In the present correlation-based model, the predicted transition onset momentum-thickness Reynolds number Re_{θ_t} is function of the turbulence intensity, based on the local free-stream velocity, and acceleration along the streamwise direction, and therefore violates Galilean invariance. According to Langtry and Menter [19], this is not problematic as long as all velocities are defined relative to the wall. To understand the influence of the non Galilean invariant terms in the prediction of transitional flows, the solution of the RANS equations written in the propeller-fixed reference frame have been compared with the solution of the RANS equations written in a earth-fixed reference frame. In the latter, this leads to an unsteady flow solution. The comparison shows that similar results are obtained between the two different formulations. Nevertheless, from similar studies on the modelling of flow transition around rotors no information is provided on how these non Galilean invariant terms are treated. Additionally, the effect of cross-flow instability as a transition mechanism is not taken into account in the RANS predictions, since the various proposed models [43–45] are not Galilean invariants due to the explicit use of the velocity vector.

2.4. Inflow Turbulence Quantities

In this section the selection of the inlet turbulence quantities for the $k-\omega$ SST turbulence and $\gamma - \tilde{\text{Re}}_{\theta_t}$ correlation-based transition models is discussed. The strong dependence of the $\gamma - \tilde{\text{Re}}_{\theta_t}$ transition model on the inlet turbulence quantities has been discussed earlier, see Eça et al. [22]. In a previous study [24], experimental streamlines obtained from paint-tests carried out at model-scale were used to obtain reference values for the prediction of the transition location. For the $k-\omega$ SST turbulence model, standard values, i.e., Tu $= 1.0\%$ and $\mu_t/\mu = 1$, were assumed as the initial and inlet turbulence quantities. The turbulence intensity at the inlet, in percent, is related to k by the relation $\text{Tu} = 100\sqrt{2k/(3U_{\text{inlet}}^2)}$, where U_{inlet} is the fluid velocity at the inlet. For the $\gamma - \tilde{\text{Re}}_{\theta_t}$ correlation-based transition model, initial and inlet values equal to Tu $= 2.5\%$ and $\mu_t/\mu = 500$ were considered, since it corresponds to the best qualitative agreement between the calculated limiting streamlines and the paint-tests carried out at $\text{Re} = 5 \times 10^5$. These values also take into account the decay of the turbulence quantities along the streamwise direction due to the distance between the inlet boundary and the propeller.

In the present study, a criterion considering the different Reynolds number regimes needs to be found for the inlet turbulence quantities. If we consider the case of a uniform flow U_∞, then the decay of the turbulence quantities is given by the following analytical solutions [46], written in the dimensionless form, of the transport equations for k and ω:

$$k^* = k^*_{\text{inlet}}\left(1+\beta(x^*-x^*_{\text{inlet}})\frac{k^*_{\text{inlet}}}{(\mu_{t\ \text{inlet}}/\mu)}\text{Re}\right)^{-\beta^*/\beta},$$
$$\omega^* = \omega^*_{\text{inlet}}\left(1+\beta(x^*-x^*_{\text{inlet}})\frac{k^*_{\text{inlet}}}{(\mu_{t\ \text{inlet}}/\mu)}\text{Re}\right)^{-1}, \quad (10)$$

where $x^* = x/L_{\text{ref}}$, $k^* = k/U^2_\infty$, $\omega^* = \omega L_{\text{ref}}/U_\infty$, k_{inlet} and ω_{inlet} are the values specified at the inlet, and L_{ref} is a reference length. In this case, the Reynolds number is defined as $\text{Re} = \rho U_\infty L_{\text{ref}}/\mu$. Equation (10) shows a strong decay, especially for the turbulence kinetic energy k; the power is about -1.087. We note that for higher Reynolds numbers, larger values of the eddy-viscosity ratio are needed to control the decay rate of the turbulence quantities.

In the present study, the same value of the inlet turbulence intensity, as found in Baltazar et al. [24], is assumed for all Reynolds numbers and the eddy-viscosity ratio is adjusted according to Equation (10) to maintain the same decay rate from the simulations at model-scale ($\text{Re} = 5\times10^5$). In this sense, the inlet eddy-viscosity ratio is specified by:

$$\frac{\mu_{t\ \text{inlet}}}{\mu} = \frac{\text{Re}}{5\times10^5}\cdot\left.\frac{\mu_{t\ \text{inlet}}}{\mu}\right|_{\text{Re}=5\times10^5}. \quad (11)$$

Table 1 presents the initial and inlet turbulence quantities assumed for the simulations at the various Reynolds numbers. We note that large values of the eddy-viscosity ratio are obtained for the higher Reynolds numbers and, at this point, it is not known how these non-realistic eddy-viscosity ratios influence the numerical solutions. Since most propeller open-water experiments are carried out at a range of Reynolds numbers between 10^5 and 10^6, a sensitivity study in the prediction of laminar-to-turbulent flow to the inlet turbulence quantities is presented for these two Reynolds numbers with both models. Furthermore, the full-scale Reynolds number, 10^7, is also analysed.

Table 1. Inlet turbulence quantities for the calculations at different Reynolds number.

Model	$k-\omega$ **SST**		$\gamma-\tilde{\text{Re}}_{\theta_t}$	
Re	**Tu**	μ_t/μ	**Tu**	μ_t/μ
1×10^4	1.0%	0.02	2.5%	10
5×10^4	1.0%	0.1	2.5%	50
1×10^5	1.0%	0.2	2.5%	100
5×10^5	1.0%	1	2.5%	500
1×10^6	1.0%	2	2.5%	1000
5×10^6	1.0%	10	2.5%	5000
1×10^7	1.0%	20	2.5%	10,000

After setting the initial and inlet turbulence quantities, Equation (11), the contribution of the Reynolds stresses as function of the Reynolds number to the momentum balance can be analysed. If we write the momentum equation, Equation (1), in the dimensionless form by taking $x^* = x/L_{\text{ref}}$, $U^* = U/U_\infty$, $V^* = V/U_\infty$, $\Omega* = \Omega L_{\text{ref}}/U_\infty$ and $P^* = P/(\rho U^2_\infty)$, we obtain:

$$\frac{\partial(V^*_j U^*_i)}{\partial x^*_j} + \varepsilon_{ijk}\Omega^*_j U^*_k = -\frac{\partial P^*}{\partial x^*_i} + \frac{\partial}{\partial x^*_j}\left[\frac{1}{\text{Re}}\left(1+\frac{\mu_t}{\mu}\right)\left(\frac{\partial U^*_i}{\partial x^*_j}+\frac{\partial U^*_j}{\partial x^*_i}\right)\right], \quad (12)$$

By combining Equations (11) and (12), we observe that the contribution of the Reynolds stresses to the momentum balance as function of the Reynolds number is maintained.

3. Solver, Propeller, Grids, Domain and Boundary Conditions

3.1. Solver

For the flow simulations, the RANS equations are discretised using a finite-volume approach with cell-centred collocated variables. A strong-conservation form and a pressure-correction equation based on the SIMPLE algorithm is used to ensure mass conservation. The implementation is face-based, which allows grids with elements consisting of an arbitrary number of faces and hanging nodes. For the convective flux terms, a second-order scheme (QUICK) is used for the momentum equations and a first-order upwind scheme is used for the $k-\omega$ SST turbulence model and the $\gamma-\tilde{\mathrm{Re}}_{\theta_t}$ transition model. The RANS equations are solved using the ReFRESCO code, which is targeted for hydrodynamic applications [47]. ReFRESCO is currently being developed within a cooperation led by MARIN. In this study, ReFRESCO version 2.1 is used.

3.2. Propeller Geometry

The marine propeller S6368 is considered in the present study. The main particulars are listed in Table 2, where R is the propeller radius. A set of experiments has been carried out at MARIN and is reported in Jonk and Willemsen [48]. This propeller was also used by Boorsma [49] to study the differences in the propeller performance due to leading-edge roughness. This propeller geometry has been used in a previous study [24] where the RANS simulations were compared to the available experimental paint-tests [49] carried out at model-scale. Therefore, as a continuation to the previous work, the same propeller geometry is selected for the present study.

Table 2. Overview of propeller particulars.

Diameter D [m]	0.2714
Chord length c at $r = 0.7R$ [m]	0.0694
Pitch P at $r = 0.7R$ [m]	0.2055
Pitch ratio P/D at $r = 0.7R$	0.757
Boss-diameter ratio	0.168
Blade-area ratio A_E/A_0	0.464
Number of blades	4

3.3. Grid Sets

Two series of six nearly-geometrically similar multi-block structured grids are generated using the commercial grid generation package GridPro [50]. The first grid series is used for the calculations at the Reynolds numbers from 1×10^4 to 5×10^5. The grids range from 1 to 35 million cells. The second grid series is used for the calculations at the Reynolds numbers from 1×10^6 to 1×10^7. The grids range from 1 to 39 million cells. Table 3 presents the number of cells in the volume and on a single blade, and the maximum and mean dimensionless wall distance of the first cell height y^+ at the Reynolds numbers 1×10^4, 5×10^5 and 1×10^7. The y^+ values correspond to the calculations using the $k-\omega$ SST turbulence model [37] at design condition. The differences between the two grid series are due to the grid space weighting in the boundary-layer region in order to obtain a $y^+ < 1$ for all Reynolds number regimes. Therefore, the boundary-layer is fully resolved and no wall functions are used. An overview of the grid with 8 million cells is presented in Figure 1.

3.4. Computational Domain and Boundary Conditions

In the simulations a cylindrical domain is considered, where the inlet, the outlet and the outer boundary are located five propeller diameters from the propeller origin. At the inlet the velocity, transition quantities, and the turbulence intensity and eddy-viscosity ratio depending on the turbulence model or transition model are prescribed, see Table 1, while the pressure is extrapolated from the interior assuming zero normal derivative. For the

outer boundary a constant pressure is specified, while a Neumann boundary condition is assumed for all other flow variables. At the outlet an outflow condition of zero downstream gradient is considered for all flow variables. At the propeller and hub surfaces, the no-split condition is enforced, where the velocity in the rotating reference frame and the turbulence kinetic energy are set equal to zero. The turbulence dissipation rate ω is specified at the near-wall cell centre according to [36], and Neumann conditions are applied to the pressure, γ and $\tilde{\mathrm{Re}}_{\theta_t}$.

Table 3. Overview of the grid sizes and number of cell faces on a single blade. Maximum and mean y^+ at Re $= 1 \times 10^4$, 5×10^5 and 1×10^7. M and k denote million and thousand, respectively.

Volume	1.0 M	2.2 M	4.3 M	8.0 M	17.8 M	34.8 M
Blade	4 k	6 k	10 k	15 k	25 k	39 k
			Re $= 1 \times 10^4$			
max y^+	0.04	0.04	0.03	0.03	0.02	0.02
mean y^+	0.01	0.01	0.01	0.00	0.00	0.00
			Re $= 5 \times 10^5$			
max y^+	0.74	0.67	0.54	0.45	0.36	0.31
mean y^+	0.23	0.18	0.13	0.11	0.08	0.06
Volume	1.4 M	3.2 M	6.1 M	11.4 M	25.0 M	39.0 M
Blade	4 k	6 k	10 k	15 k	25 k	39 k
			Re $= 1 \times 10^7$			
max y^+	0.34	0.26	0.20	0.16	0.12	0.10
mean y^+	0.10	0.08	0.06	0.05	0.04	0.03

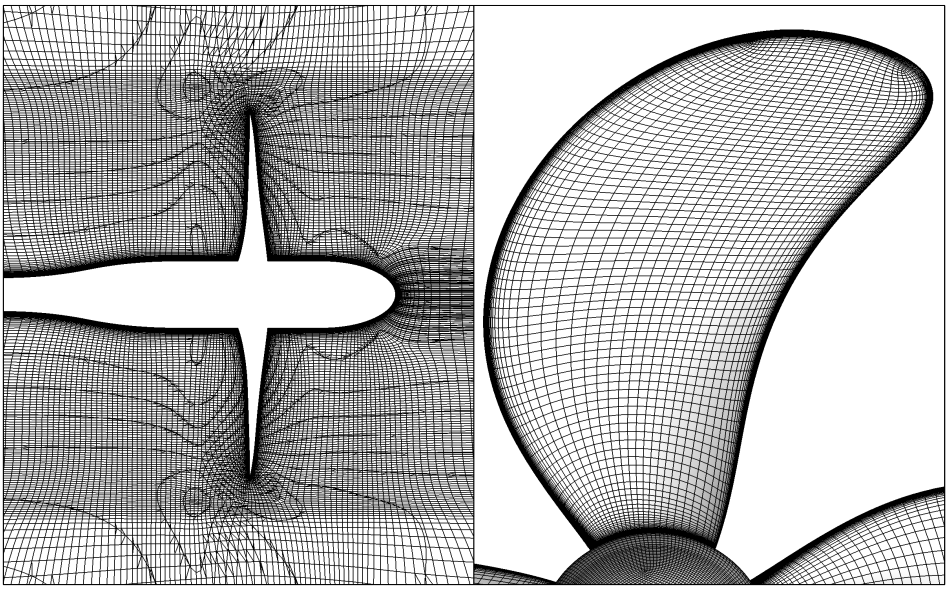

Figure 1. Overview of the grid around propeller and blades. Grid with 8.0 M cells.

4. Results

4.1. General

Results are presented for the marine propeller S6368 in open-water conditions. The operating conditions are defined by the advance coefficient $J = U/(nD)$, where U is the propeller advance speed, D the propeller diameter and $n = \Omega/(2\pi)$ is the rotation rate in rps. The open-water characteristics are expressed by the thrust coefficient $K_T = T/(\rho n^2 D^4)$, torque coefficient $K_Q = Q/(\rho n^2 D^5)$ and open-water efficiency $\eta_0 = JK_T/(2\pi K_Q)$, where T

is the propeller thrust and Q the propeller torque. Other useful quantities are the pressure coefficient C_p and the skin friction coefficient C_f defined as:

$$C_p = \frac{p - p_\infty}{1/2\rho V_{\text{ref}}^2}, \quad C_f = \frac{\tau_w}{1/2\rho U^2}, \tag{13}$$

where p_∞ is the undisturbed static pressure here defined at the inlet boundary, τ_w is the local wall shear stress and $V_{\text{ref}} = \sqrt{U^2 + (\Omega r)^2}$ is a reference velocity defined as the undisturbed onset velocity at the radial position r.

Simulations are carried out at $J = 0.568$ (near design condition) for a range of Reynolds numbers between 1×10^4 to 1×10^7, which cover different flow regimes, i.e., from fully laminar to turbulent flow. The Reynolds number is defined based on the propeller blade chord length at $0.7R$, $c_{0.7R}$, and the resulting onset velocity at that radius:

$$\text{Re} = \frac{\rho c_{0.7R} \sqrt{U^2 + (n\pi 0.7D)^2}}{\mu}. \tag{14}$$

For the flow computations, the same geometrical scale is used as for the model-scale simulations, i.e., $\text{Re} = 5 \times 10^5$, and the variation of the Reynolds number is achieved by adapting the propeller rotation rate n.

4.2. Estimation of Numerical Errors

In this section the numerical errors that occur in the calculations are analysed. The numerical errors involved in every computing simulation can be divided into three types [51]: round-off error, iterative error and discretisation error.

Since double-precision is used in the present calculations, the round-off error is neglected. The iterative error, which occurs due to the iterative solution of the transport equations, is monitored with the infinity norm L_∞ and L_2 norm of the residuals,

$$\begin{aligned} L_\infty(\phi) &= \max|\text{res}(\phi_i)|, \quad 1 \le i \le N_{\text{cells}}, \\ L_2(\phi) &= \sqrt{\sum_{i=1}^{N_{\text{cells}}} \text{res}^2(\phi_i) \Big/ N_{\text{cells}}} \end{aligned} \tag{15}$$

in which $\text{res}(\phi_i)$ stands for the residual of any local flow quantity and N_{cells} is the total number of grid cells. The iterative convergence at $J = 0.568$ using the $k-\omega$ SST turbulence model and $\gamma - \tilde{\text{Re}}_{\theta_t}$ transition model is presented in Figures 2 and 3, respectively. The local flow quantities considered are the Cartesian components of the flow velocity $U_{X,Y,Z}$, the modified static pressure P, the turbulence kinetic energy k, the specific turbulence dissipation rate ω, the intermittency γ and the local transition onset momentum thickness Reynolds number $\tilde{\text{Re}}_{\theta_t}$. The results refer to the grids with 17.8 million cells, for $\text{Re} = 1 \times 10^4$ and 5×10^5, and 11.4 million cells, for $\text{Re} = 1 \times 10^7$. In this study a convergence criterion of 10^{-6} is adopted for the L_∞ and L_2 norms of the local variables. The analysis of the results for $\text{Re} = 1 \times 10^4$ show that this convergence criterion is achieved for all quantities, with the exception of the turbulence dissipation rate ω in the simulation using the $k-\omega$ SST turbulence model, where the residual stagnates at approximately 10^{-5}. For the Reynolds number 5×10^5, iterative convergence is only obtained with the $k-\omega$ SST turbulence model. With the $\gamma - \tilde{\text{Re}}_{\theta_t}$ transition model, convergence of the flow quantities is difficult to achieve, especially for intermittency γ, where the residual stagnates between 0.1 and 1. For the Reynolds number 1×10^7, a similar behaviour is observed for both models, since the residuals stagnate with the number of iterations. We note that for the simulations carried out with the $k-\omega$ SST turbulence model, the L_2 norm of the residuals is lower than 10^{-6} for all flow quantities. This result shows that the maximum residuals have a minor contribution to the global iterative error and it occurs locally at the trailing-edge near the blade tip. With the $\gamma - \tilde{\text{Re}}_{\theta_t}$ transition model, the large residuals observed in the

intermittency occur at the blade mid-chord and leading-edge for Re $= 5 \times 10^5$ and 1×10^7, respectively. These locations coincide with the predicted transition region, suggesting that denser grids may be needed in these regions. With the exception of the intermittency, L_2 norm of the residuals lower than 10^{-6} is obtained for the remaining flow quantities. In addition, the iterative convergence of the propeller thrust and torque coefficients is plotted in Figure 4. Convergence is obtained for all cases, preceding the criterion of 10^{-6} and the stagnation of the residuals. These results suggest a negligible effect of the iterative error on the propeller forces.

The discretization error, due to the discretization of both the mathematical model and domain, is estimated following the procedure described in Eça and Hoekstra [52]. In this procedure, the discretization error ϵ is estimated by the equation:

$$\epsilon = \phi_i - \phi_0 = \alpha h_i^p, \tag{16}$$

in which ϕ_i stands for any integral or local flow quantity, ϕ_0 is the estimate of the exact solution, α a constant, p is the observed order of accuracy and h_i is the typical cell size of grid i, determined in our case from the total number of grid cells N_{cells} by $h_i = (1/N_{\text{cells}})^{1/3}$. The unknown coefficients in Equation (16) are determined from a least-square fit of the numerical solutions on systematically refined grids. The error estimate is then converted into an numerical uncertainty U_{num} that depends on the observed order of accuracy and on the standard deviation of the fit.

The convergence of the thrust and torque coefficients with the grid refinement ratio h_i/h_1 is presented in Figure 5. The plots include also the fits for each model and Reynolds number. An apparent order of convergence between 1.17 and 1.59 is obtained for the simulations at Re $= 1 \times 10^4$. For the other Reynolds number regimes, second-order convergence is achieved from the least-square fit, with the exception of the thrust coefficient predicted by the $k-\omega$ SST turbulence model at Re $= 1 \times 10^7$, where an apparent order of convergence equal to 1.84 is obtained. However, not all cases show monotonic convergence. Different estimations of the exact solution are observed from the comparison between the turbulence and transition models at the Reynolds number regimes Re $= 5 \times 10^5$ and 1×10^7. The estimated numerical uncertainties are of the order of 0.4–4.2%. We note that the $\gamma - \tilde{\text{Re}}_{\theta_t}$ transition model was not able to converge for the coarser grids at Re $= 1 \times 10^7$. Finally, the variation of the open-water quantities in comparison to the finest grid is presented in Table 4, where a reduction with the increase of the number of cells is observed. For practical purposes, the grid with 17.8 million cells is chosen in the subsequent studies for the Reynolds numbers between 1×10^4 and 5×10^5, since its variation to the finest grid is lower than 1.0%. For the Reynolds numbers between 1×10^6 and 1×10^7, the grid with 11 million cells is used.

Table 4. Variation of the force coefficients with grid density compared to the finest grid at $J = 0.568$. Re $= 1 \times 10^4$, 5×10^5 and 1×10^7. M denotes million.

	$k-\omega$ SST			$\gamma - \tilde{\text{Re}}_{\theta_t}$		
Grid	ΔK_T	ΔK_Q	$\Delta \eta_0$	ΔK_T	ΔK_Q	$\Delta \eta_0$
			Re $= 1 \times 10^4$			
1.0 M	9.6%	8.3%	1.1%	9.3%	8.3%	1.1%
2.2 M	6.5%	5.0%	1.4%	6.3%	5.0%	1.4%
4.3 M	4.0%	3.0%	0.8%	3.8%	3.0%	0.8%
8.0 M	2.5%	1.8%	0.6%	2.4%	1.8%	0.6%
17.8 M	0.0%	0.6%	0.3%	0.9%	0.6%	0.2%
			Re $= 5 \times 10^5$			
1.0 M	3.2%	4.7%	−1.4%	1.3%	5.4%	−3.9%
2.2 M	1.7%	2.2%	−0.5%	0.4%	2.8%	−2.3%
4.3 M	0.9%	1.2%	−0.3%	0.1%	1.7%	−1.6%
8.0 M	0.5%	0.7%	−0.2%	−0.1%	0.9%	−1.0%
17.8 M	0.0%	0.1%	−0.1%	−0.2%	0.1%	−0.3%

Table 4. *Cont.*

	$k-\omega$ SST			$\gamma-\tilde{\mathrm{Re}}_{\theta_t}$		
Grid	ΔK_T	ΔK_Q	$\Delta\eta_0$	ΔK_T	ΔK_Q	$\Delta\eta_0$
			$\mathrm{Re}=1\times10^7$			
1.4 M	1.4%	4.3%	−2.7%	–	–	–
3.2 M	0.7%	2.1%	−1.4%	–	–	–
6.1 M	0.5%	1.3%	−0.8%	0.5%	1.4%	−0.9%
11.4 M	0.3%	0.7%	−0.5%	0.3%	0.8%	−0.5%
25.0 M	−0.1%	0.0%	0.0%	−0.1%	0.0%	−0.2%

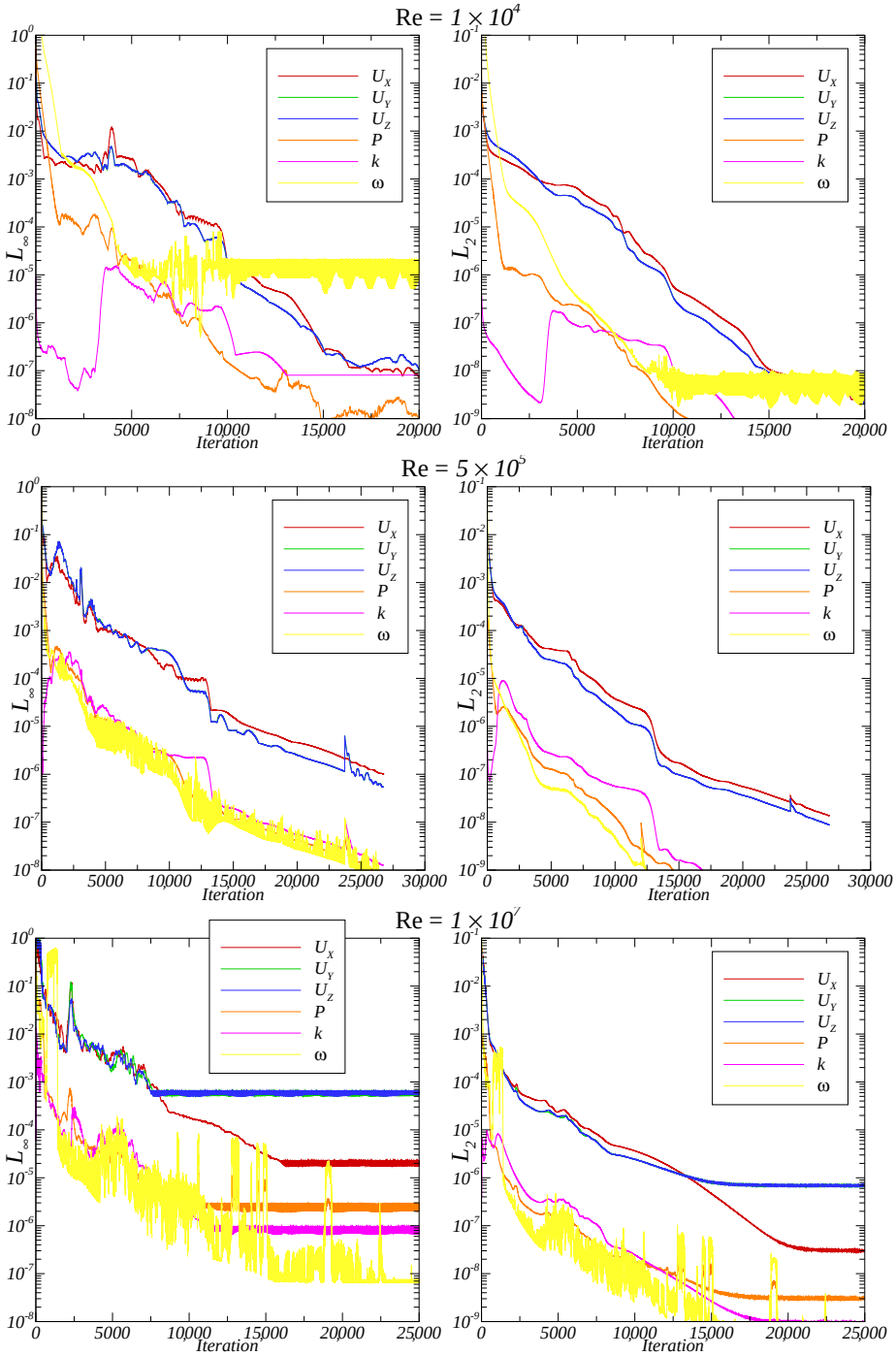

Figure 2. L_∞ (**left**) and L_2 (**right**) iterative convergence at $J = 0.568$ using the $k-\omega$ SST turbulence model. $\mathrm{Re} = 1\times10^4$ (**top**), 5×10^5 (**middle**) and 1×10^7 (**bottom**).

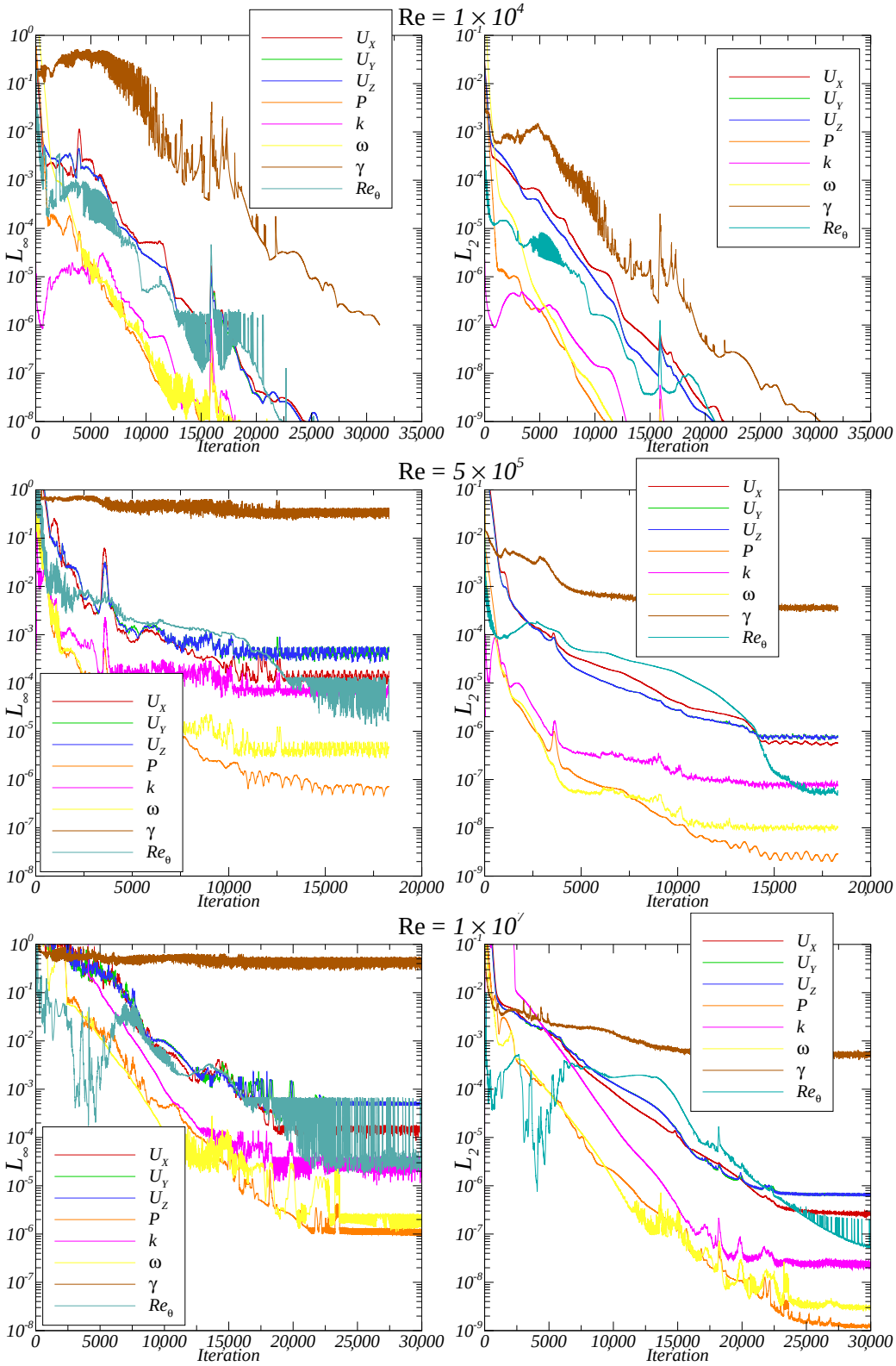

Figure 3. L_∞ (**left**) and L_2 (**right**) iterative convergence at $J = 0.568$ using the $\gamma - \tilde{\mathrm{Re}}_{\theta_t}$ transition model. $\mathrm{Re} = 1 \times 10^4$ (**top**), 5×10^5 (**middle**) and 1×10^7 (**bottom**).

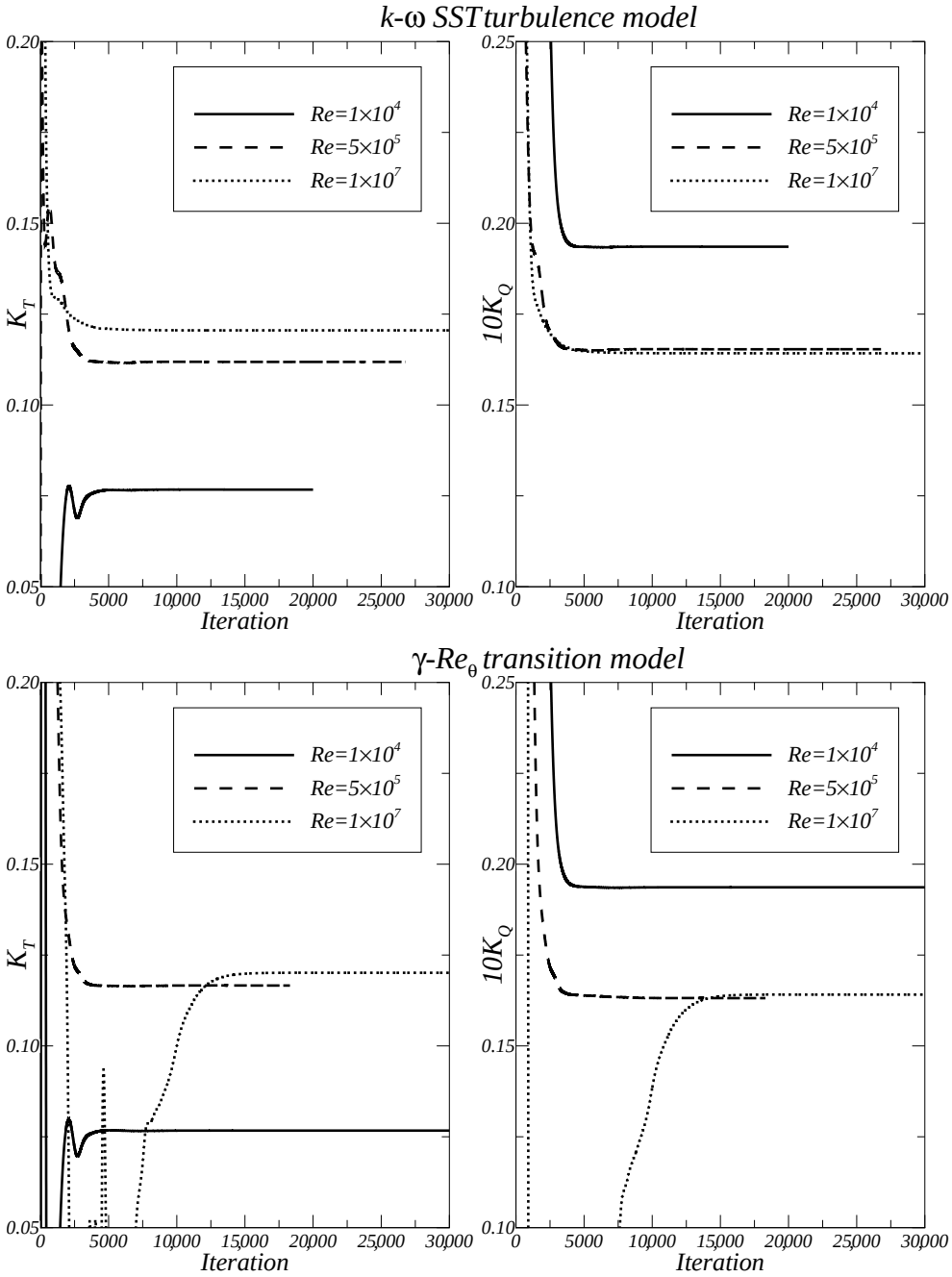

Figure 4. Iterative convergence of K_T (**left**) and $10K_Q$ (**right**) at $J = 0.568$ using the $k-\omega$ SST turbulence model (**top**) and $\gamma - \tilde{\mathrm{Re}}_{\theta_t}$ transition model (**bottom**).

4.3. Influence of Inlet Turbulence Quantities

Since large eddy-viscosity ratios are obtained for the different Reynolds numbers to maintain the decay rate of the turbulence quantities, Table 1, the effect of the inlet turbulence quantities in the prediction of laminar-to-turbulent flow transition is analysed. Results are presented for the turbulence and transition models at the Reynolds numbers of 10^5, 10^6 and 10^7. For the $k-\omega$ SST turbulence model, a standard value is assumed for the turbulence intensity, i.e Tu = 1.0%. For the eddy-viscosity ratio, the ratio of 1 is compared with 500 and the obtained ratio from Equation (11). For the $\gamma - \tilde{\mathrm{Re}}_{\theta_t}$ transition model, the standard values (Tu = 1.0% and $\mu_t/\mu = 1$) are compared with Tu = 2.5% and the $\mu_t/\mu = 500$ and the values obtained from Equation (11). The influence of inlet turbulence quantities is analysed by comparing the skin friction coefficient and orientation of the limiting streamlines in Figures 6–13, and the propeller force coefficients and levels of the

turbulence quantities near the propeller region in Tables 5–7. The location of the transition region is identified by the increase in the skin friction distribution and the change in the orientation of the limiting streamlines from the radial direction (associated with laminar flow) towards the chordwise directions (associated with turbulent flow).

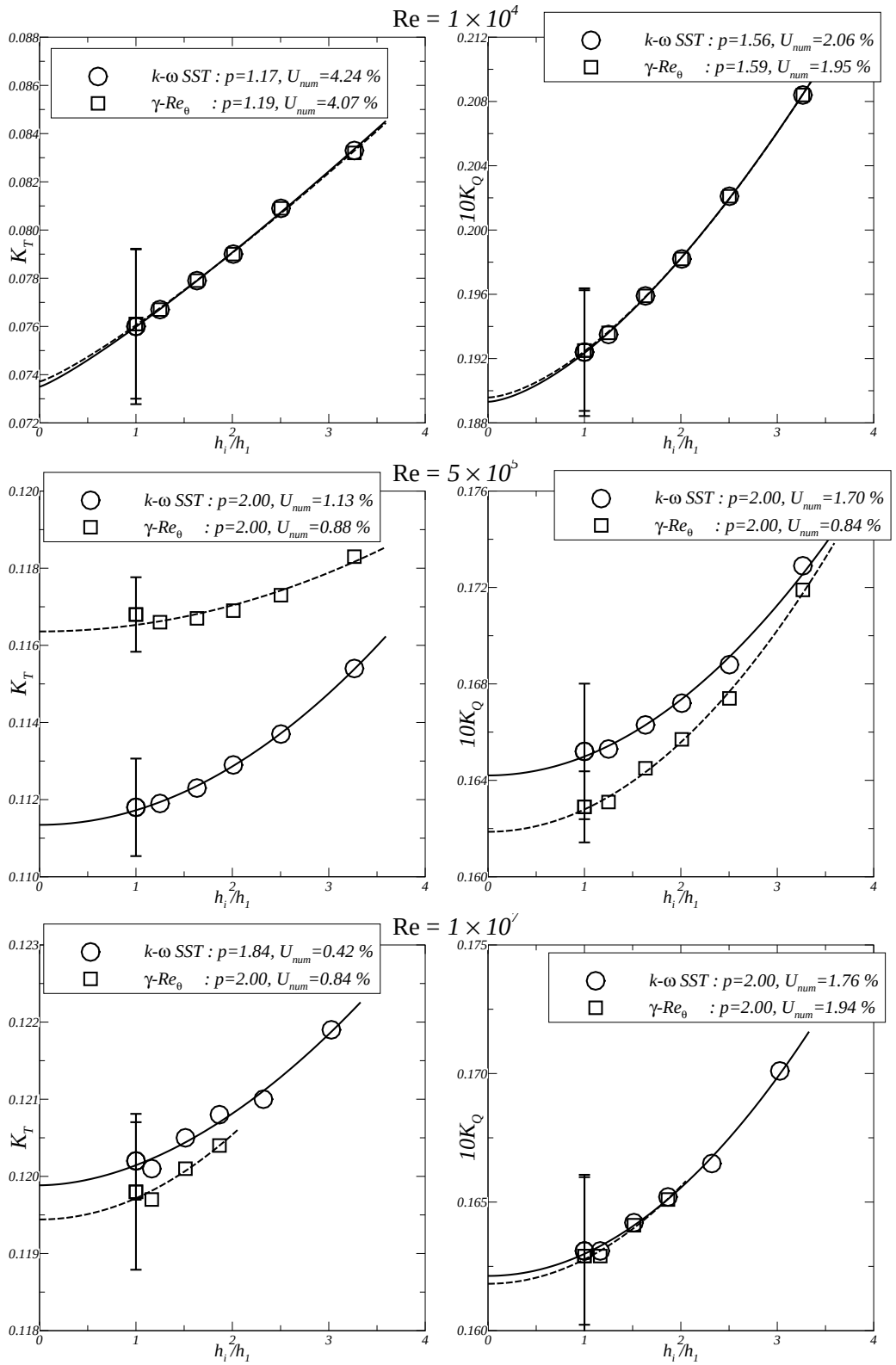

Figure 5. Convergence of K_T (**left**) and $10K_Q$ (**right**) with the grid refinement ratio h_i/h_1 at $J = 0.568$: $\mathrm{Re} = 1 \times 10^4$ (**top**), 5×10^5 (**middle**) and 1×10^7 (**bottom**).

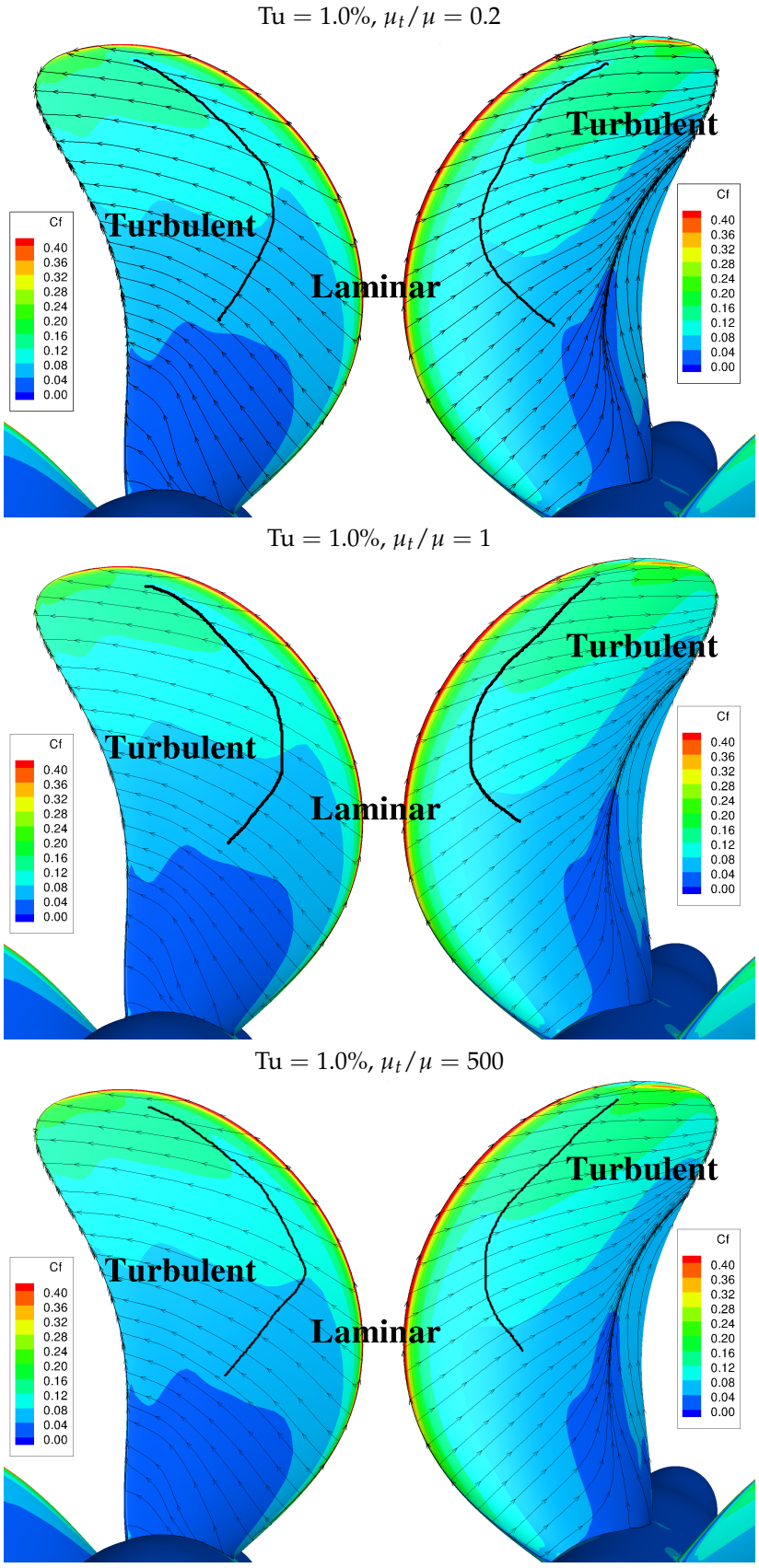

Figure 6. Influence of the inlet turbulence quantities on the propeller blade flow. Limiting streamlines and skin friction coefficient using the $k-\omega$ SST turbulence model at Re $= 1 \times 10^5$ for $J = 0.568$. Pressure side (**left**) and suction side (**right**).

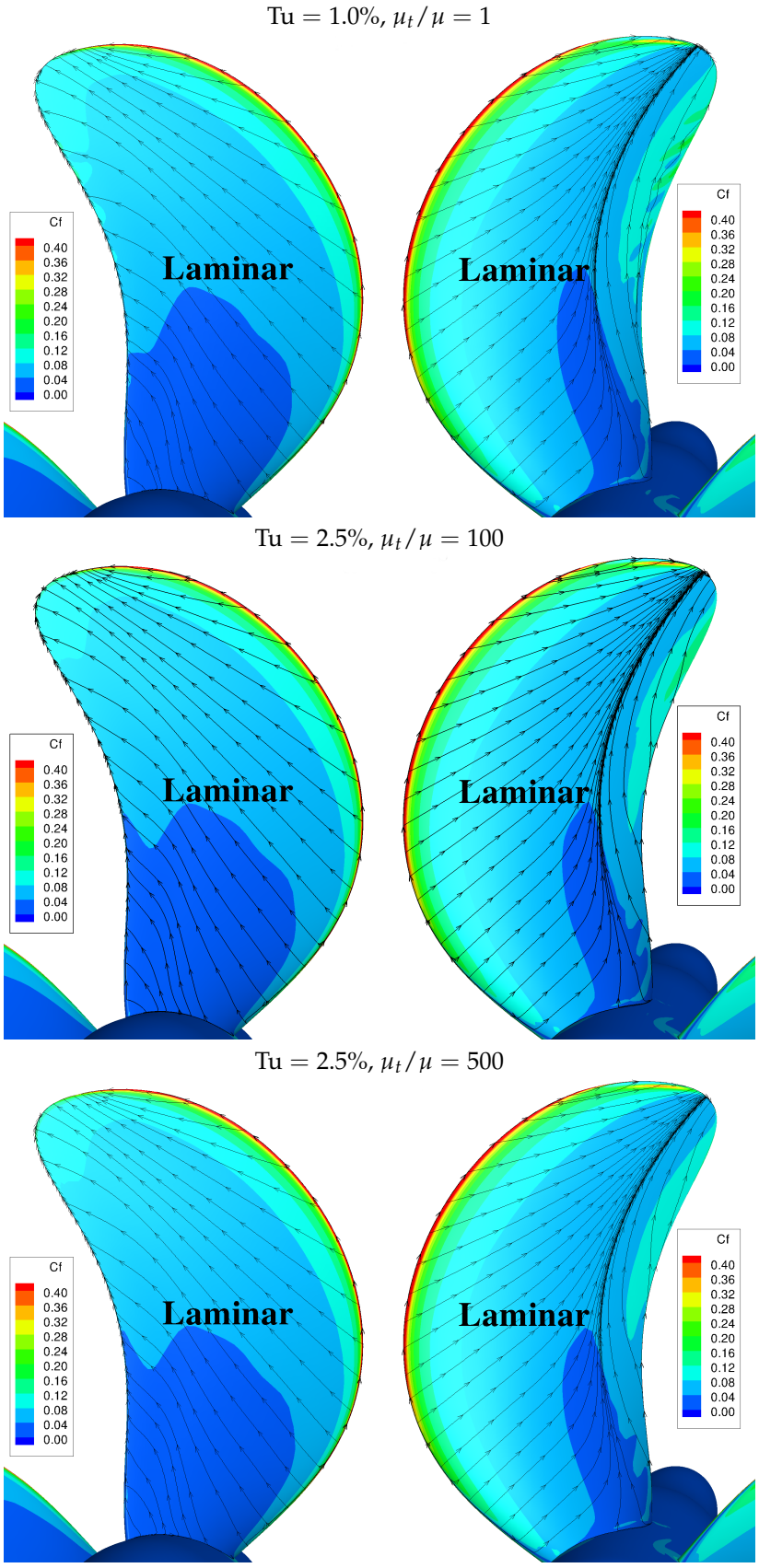

Figure 7. Influence of the inlet turbulence quantities on the propeller blade flow. Limiting streamlines and skin friction coefficient using the $\gamma - \tilde{\mathrm{Re}}_{\theta_t}$ transition model at $\mathrm{Re} = 1 \times 10^5$ for $J = 0.568$. Pressure side (**left**) and suction side (**right**).

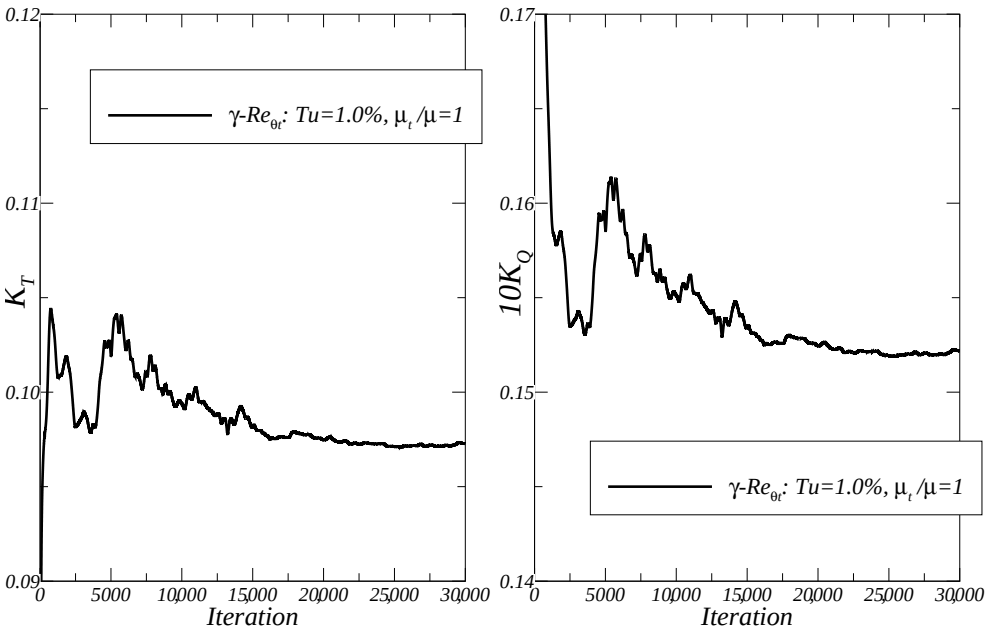

Figure 8. Iterative convergence of K_T (**left**) and $10K_Q$ (**right**) at $J = 0.568$ using the $\gamma - \tilde{\mathrm{Re}}_{\theta_t}$ transition model at $\mathrm{Re} = 1 \times 10^5$ with Tu = 1.0% and $\mu_t/\mu = 1$ for $J = 0.568$.

Table 5. Influence of the inlet turbulence quantities on the propeller forces at $\mathrm{Re} = 1 \times 10^5$ for $J = 0.568$. Turbulence intensity at $x/R = 1$ refers to section $r/R = 0.7$.

Inlet $x/R = 10$		**$x/R = 1$**		**Forces**	
Tu	**μ_t/μ**	**Tu**	**μ_t/μ**	**K_T**	**$10K_Q$**
$k - \omega$ SST					
1.0%	0.2	0.2%	0.15	0.1041	0.1655
1.0%	1	0.4%	0.86	0.1046	0.1674
1.0%	500	1.0%	29.6	0.1046	0.1678
$\gamma - \tilde{\mathrm{Re}}_{\theta_t}$					
1.0%	1	0.4%	0.85	–	–
2.5%	100	2.1%	97.6	0.1099	0.1675
2.5%	500	2.4%	166.2	0.1110	0.1693

Table 6. Influence of the inlet turbulence quantities on the propeller forces at $\mathrm{Re} = 1 \times 10^6$ for $J = 0.568$. Turbulence intensity at $x/R = 1$ refers to section $r/R = 0.7$.

Inlet $x/R = 10$		**$x/R = 1$**		**Forces**	
Tu	**μ_t/μ**	**Tu**	**μ_t/μ**	**K_T**	**$10K_Q$**
$k - \omega$ SST					
1.0%	1	0.1%	0.74	0.1150	0.1661
1.0%	2	0.2%	1.55	0.1149	0.1660
1.0%	500	0.9%	247.4	0.1149	0.1661
$\gamma - \tilde{\mathrm{Re}}_{\theta_t}$					
1.0%	1	0.1%	0.74	–	–
1.0%	500	0.9%	232.9	0.1246	0.1624
2.5%	500	1.9%	478.3	0.1176	0.1662
2.5%	1000	2.1%	975.5	0.1173	0.1664

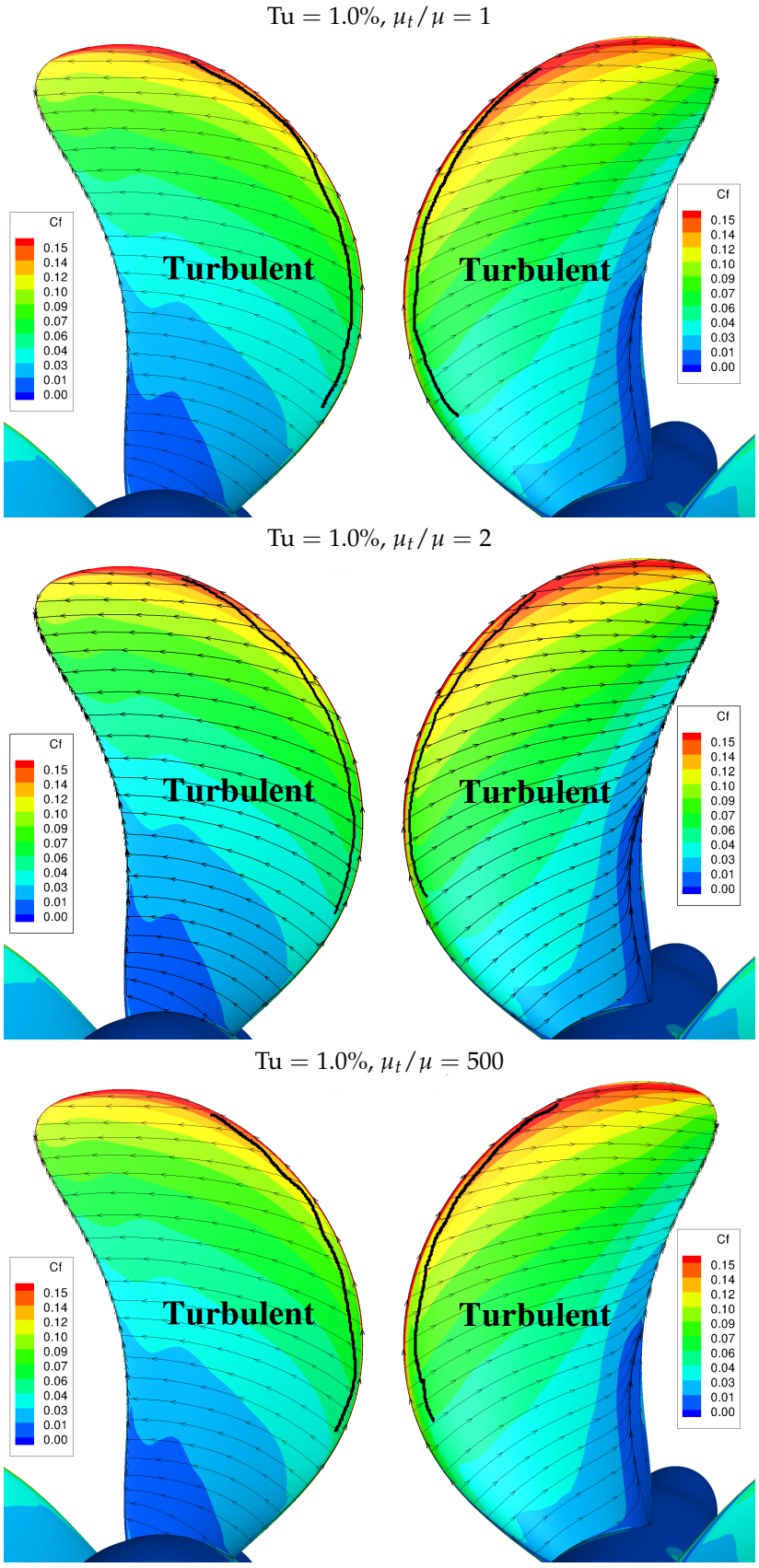

Figure 9. Influence of the inlet turbulence quantities on the propeller blade flow. Limiting streamlines and skin friction coefficient using the $k-\omega$ SST turbulence model at Re $= 1 \times 10^6$ for $J = 0.568$. Pressure side (**left**) and suction side (**right**).

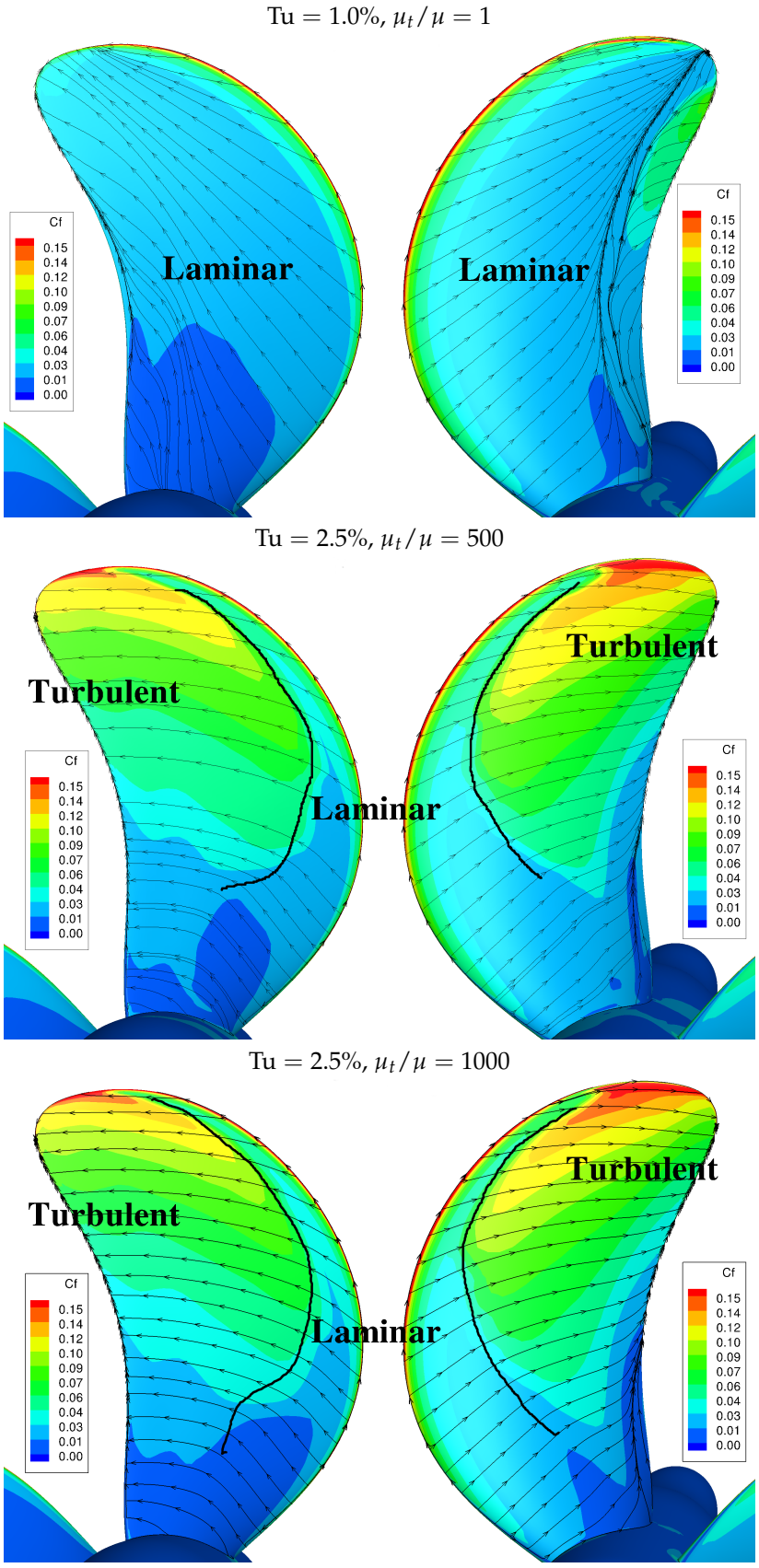

Figure 10. Influence of the inlet turbulence quantities on the propeller blade flow. Limiting streamlines and skin friction coefficient using the $\gamma - \tilde{\mathrm{Re}}_{\theta_t}$ transition model at $\mathrm{Re} = 1 \times 10^6$ for $J = 0.568$. Pressure side (**left**) and suction side (**right**).

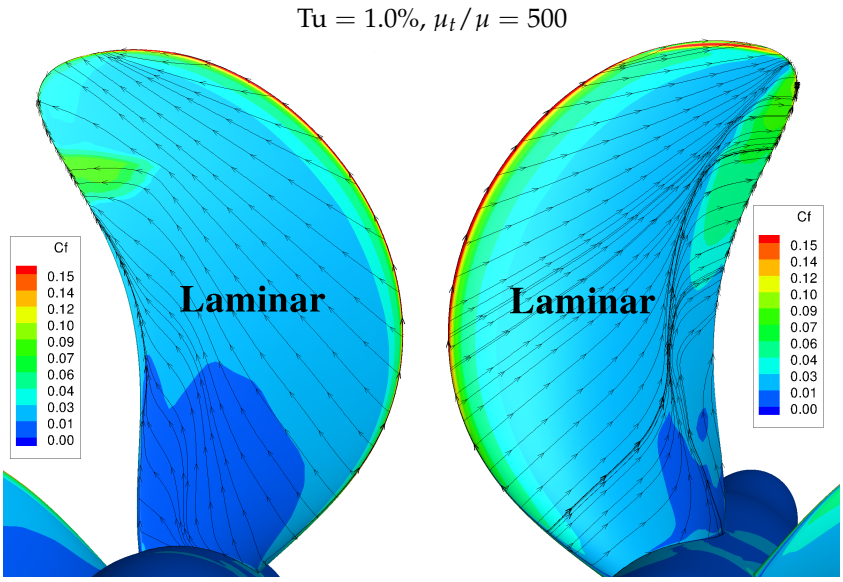

Figure 11. Influence of the inlet turbulence quantities on the propeller blade flow. Limiting streamlines and skin friction coefficient using the $\gamma - \tilde{\mathrm{Re}}_{\theta_t}$ transition model at $\mathrm{Re} = 1 \times 10^6$ for $J = 0.568$. Pressure side (**left**) and suction side (**right**).

Table 7. Influence of the inlet turbulence quantities on the propeller forces at $\mathrm{Re} = 1 \times 10^7$ for $J = 0.568$. Turbulence intensity at $x/R = 1$ refers to section $r/R = 0.7$.

Inlet $x/R = 10$		**$x/R = 1$**		**Forces**	
Tu	**μ_t/μ**	**Tu**	**μ_t/μ**	**K_T**	**$10K_Q$**
$k - \omega$ SST					
1.0%	1	0.04%	0.7	0.1205	0.1642
1.0%	20	0.2%	15.5	0.1205	0.1642
1.0%	500	0.7%	470.3	0.1205	0.1642
$\gamma - \tilde{\mathrm{Re}}_{\theta_t}$					
1.0%	1	0.04%	0.7	0.1240	0.1651
2.5%	500	0.8%	423.0	0.1204	0.1639
2.5%	10,000	2.1%	9765.6	0.1201	0.1641

Results show a negligible effect of the inlet turbulence quantities on the blade boundary-layer flow and propeller forces with the $k - \omega$ SST turbulence model. From the comparison with the $\gamma - \tilde{\mathrm{Re}}_{\theta_t}$ transition model simulations, flow transition is predicted at the lower Reynolds number, whereas turbulent flow is obtained at 1×10^6 and 1×10^7.

From the analysis of the $\gamma - \tilde{\mathrm{Re}}_{\theta_t}$ transition model predictions, fully laminar flow is obtained for the Reynolds number 1×10^5. In this case, a negligible effect of the inlet turbulence quantities is also obtained. However, iterative convergence of the equations is difficult to obtain when using the standard values (Tu = 1.0% and $\mu_t/\mu = 1$), as observed in the variation of the thrust and torque coefficients (Figure 8).

For the Reynolds number of 1×10^6, a strong influence of the inlet turbulence quantities in the location of the laminar-to-turbulent transition is observed. Once again, iterative convergence is not obtained with Tu = 1.0% and $\mu_t/\mu = 1$. In this comparison, results are also presented for the case with Tu = 1.0% and $\mu_t/\mu = 500$ in Figure 11. In this case, a strong influence of the turbulence intensity on the transition location is seen, whereas the change in the eddy-viscosity ratio between 500 and 1000 presents a small effect in the extend of the laminar flow region. From the comparison between $\mu_t/\mu = 500$ and 1000, small differences in the extend of the laminar flow region and propeller forces are observed. For the full-scale Reynolds number, 1×10^7, a turbulent flow regime with a small laminar flow region near the leading-edge is obtained for $\mu_t/\mu = 500$ and 10,000.

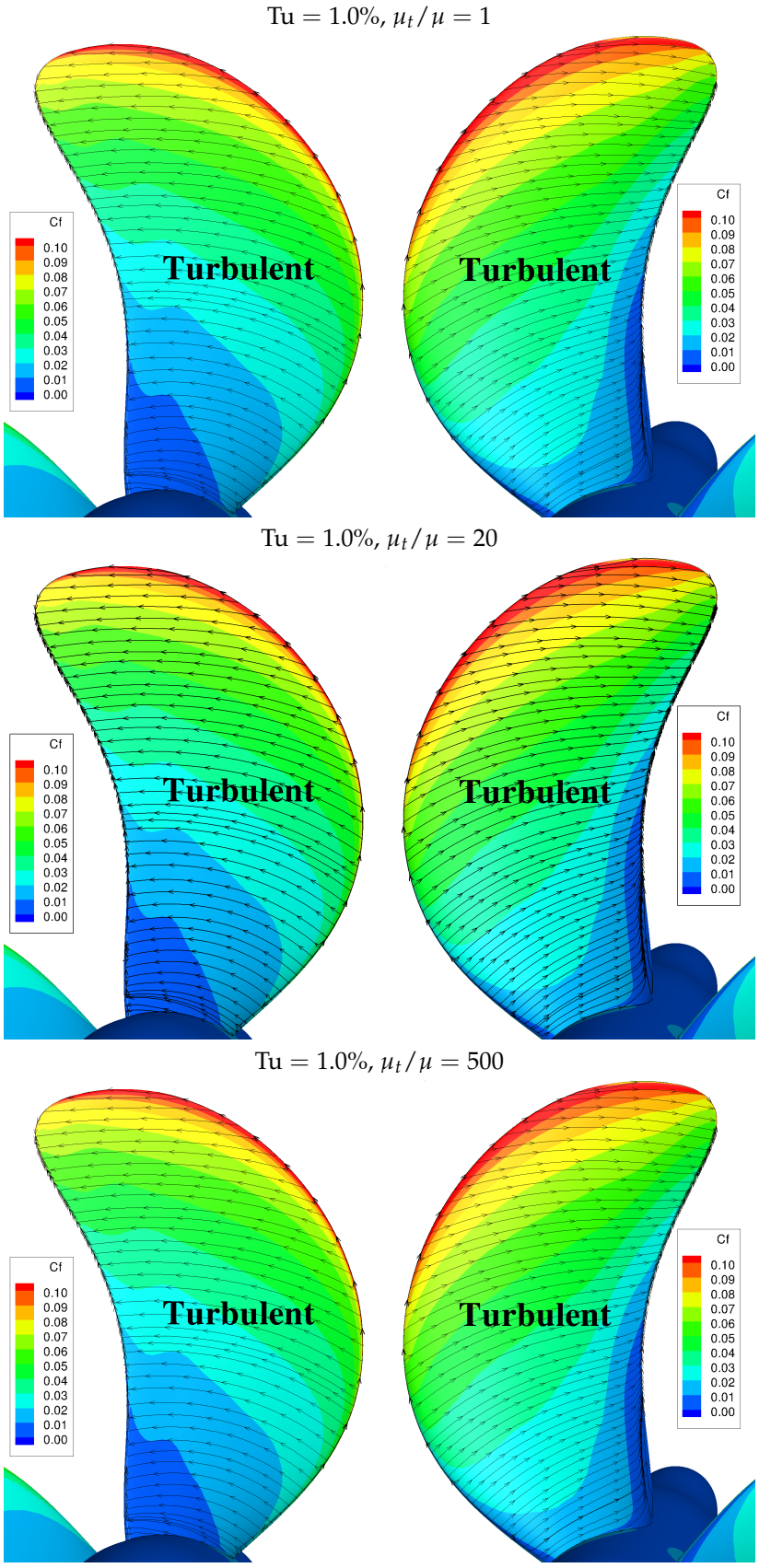

Figure 12. Influence of the inlet turbulence quantities on the propeller blade flow. Limiting streamlines and skin friction coefficient using the $k-\omega$ SST turbulence model at Re $= 1 \times 10^7$ for $J = 0.568$. Pressure side (**left**) and suction side (**right**).

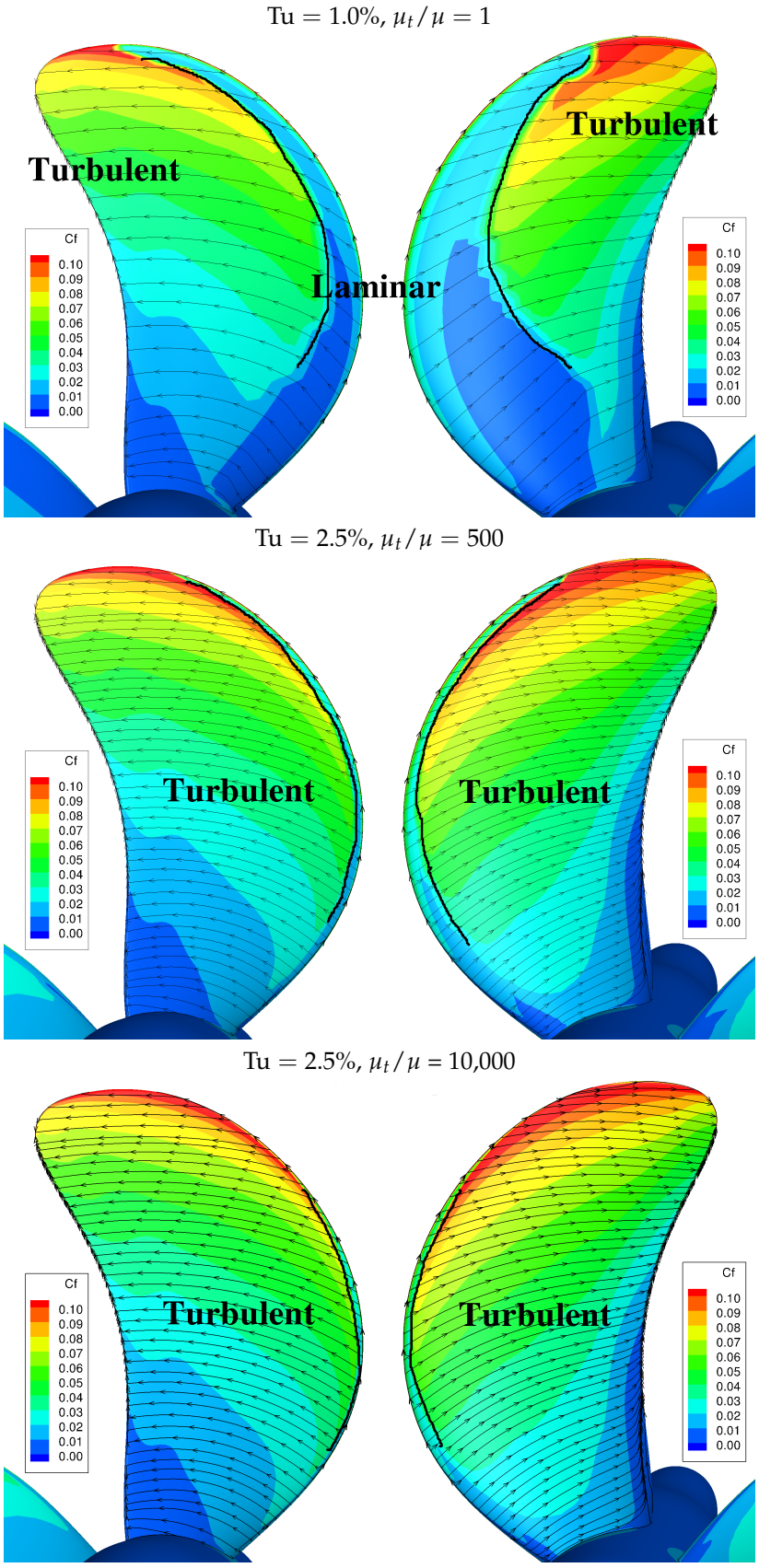

Figure 13. Influence of the inlet turbulence quantities on the propeller blade flow. Limiting streamlines and skin friction coefficient using the $\gamma - \tilde{\mathrm{Re}}_{\theta_t}$ transition model at $\mathrm{Re} = 1 \times 10^7$ for $J = 0.568$. Pressure side (**left**) and suction side (**right**).

This comparison shows the importance of the inlet turbulence quantities on the prediction of the flow at different Reynolds numbers. If the flow is fully laminar or turbulent the selection of inlet turbulent quantities shows a negligible effect on the propeller blade flow. However, flow transition occurs at 5×10^5 [24] and 1×10^6, and therefore the selection of inlet turbulence quantities is crucial for an accurate prediction of the propeller blade flow. Since it is not straightforward to obtain reference values that can be used for a given type of flow, the inlet values have been calibrated from the comparison with paint-tests and the eddy-viscosity ratio is adjusted to control the decay of the turbulence intensity from the inlet to the propeller region. In addition, Equation (11) offers an alternative for blind predictions at model-scale using the $\gamma - \tilde{\mathrm{Re}}_{\theta_t}$ transition model. In this study, the inlet turbulence quantities defined in Table 1 are considered for the analysis of the flow and prediction of the scale-effects.

4.4. Flow Analysis

In this section the propeller flow predictions at different Reynolds number regimes are analysed. Figures 14–19 present the limiting streamlines and skin friction distribution on the pressure and suction sides of the blade for different Reynolds numbers at $J = 0.568$, predicted by the $k - \omega$ SST turbulence model and $\gamma - \tilde{\mathrm{Re}}_{\theta_t}$ transition model. The domains of laminar and turbulent flow are identified in the figures based on the orientation of the limiting streamlines and skin friction distribution over the blade surface.

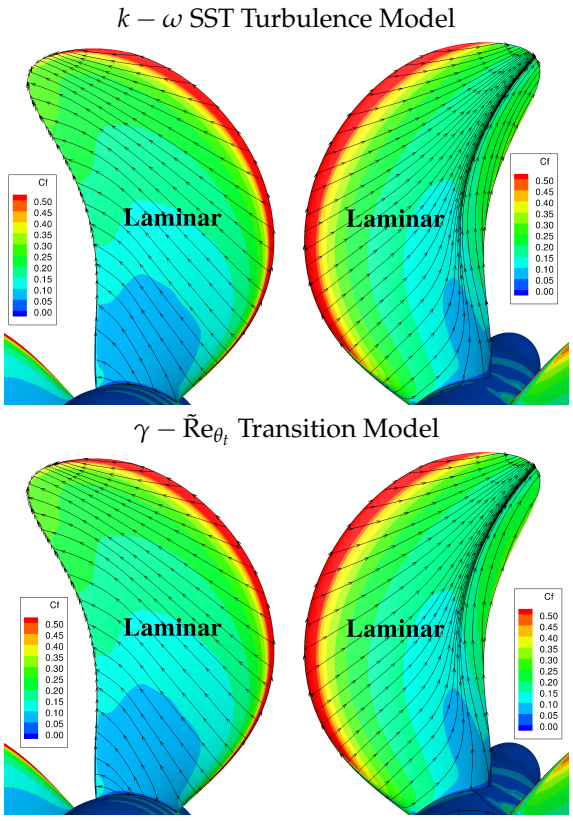

Figure 14. Limiting streamlines and skin friction coefficient using the $k - \omega$ SST turbulence model (**top**) and $\gamma - \tilde{\mathrm{Re}}_{\theta_t}$ transition model (**bottom**) at $\mathrm{Re} = 1 \times 10^4$ for $J = 0.568$. Pressure side (**left**) and suction side (**right**).

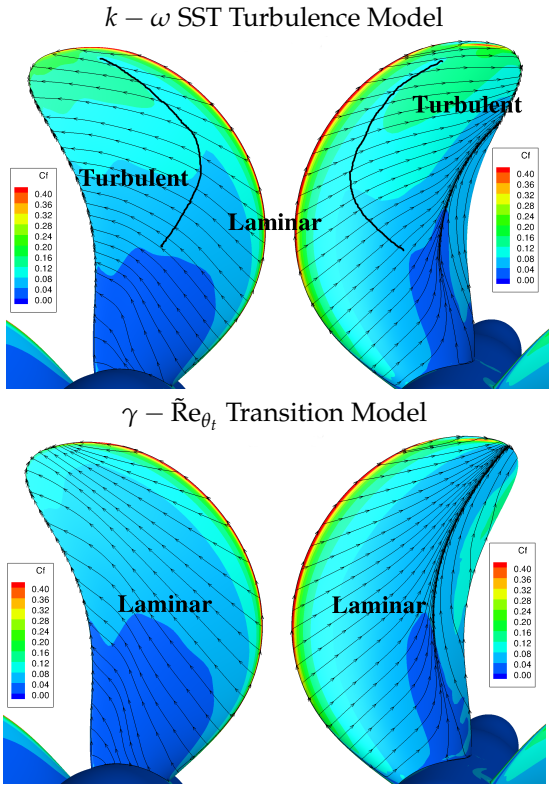

Figure 15. Limiting streamlines and skin friction coefficient using the $k-\omega$ SST turbulence model (**top**) and $\gamma-\tilde{\mathrm{Re}}_{\theta_t}$ transition model (**bottom**) at $\mathrm{Re}=1\times10^5$ for $J=0.568$. Pressure side (**left**) and suction side (**right**).

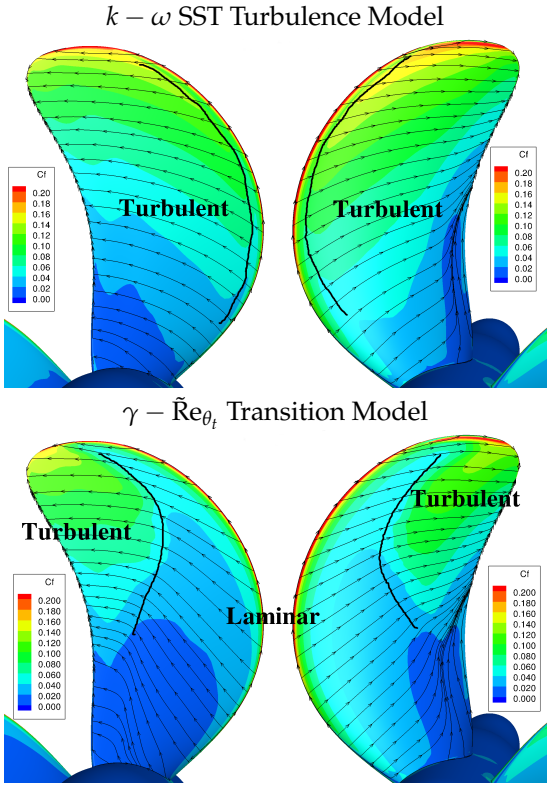

Figure 16. Limiting streamlines and skin friction coefficient using the $k-\omega$ SST turbulence model (**top**) and $\gamma-\tilde{\mathrm{Re}}_{\theta_t}$ transition model (**bottom**) at $\mathrm{Re}=5\times10^5$ for $J=0.568$. Pressure side (**left**) and suction side (**right**).

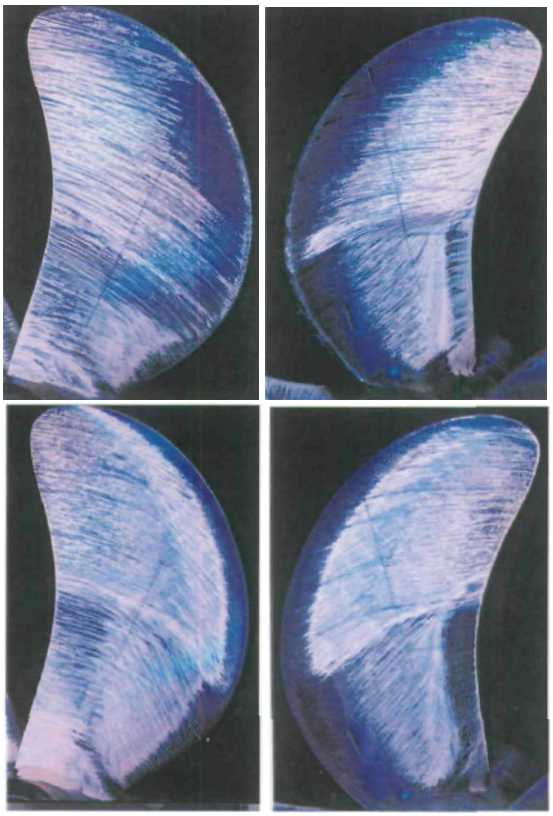

Figure 17. Propeller paint-tests with (**top**) and without leading-edge roughness (**bottom**) at $\mathrm{Re} = 5 \times 10^5$ for $J = 0.568$ [49].

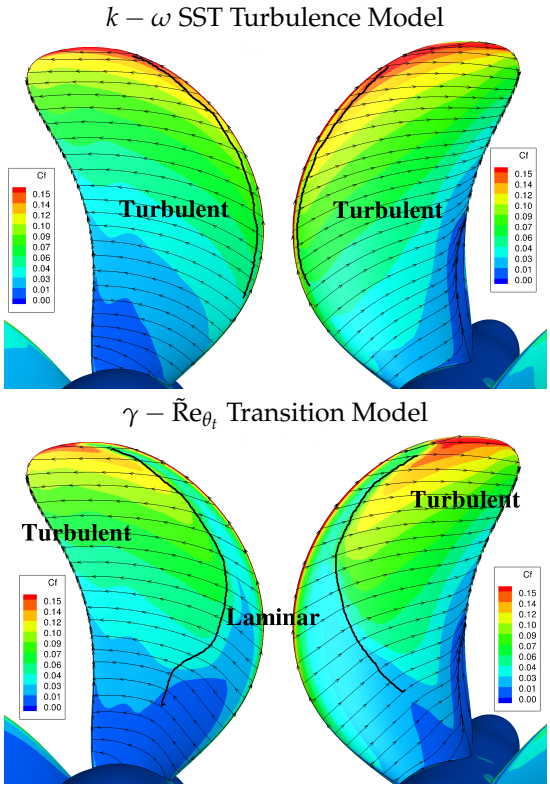

Figure 18. Limiting streamlines and skin friction coefficient using the $k - \omega$ SST turbulence model (**top**) and $\gamma - \tilde{\mathrm{Re}}_{\theta_t}$ transition model (**bottom**) at $\mathrm{Re} = 1 \times 10^6$ for $J = 0.568$. Pressure side (**left**) and suction side (**right**).

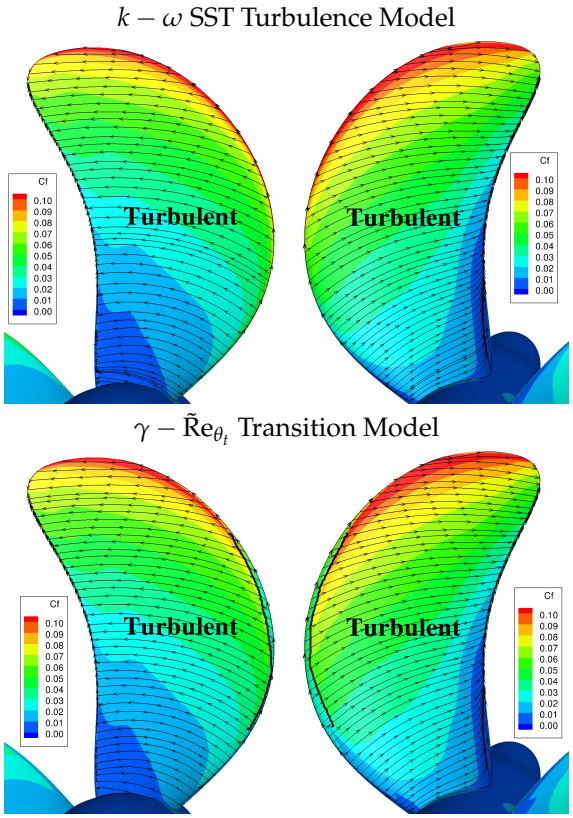

Figure 19. Limiting streamlines and skin friction coefficient using the $k-\omega$ SST turbulence model (**top**) and $\gamma - \tilde{\mathrm{Re}}_{\theta_t}$ transition model (**bottom**) at $\mathrm{Re} = 1 \times 10^7$ for $J = 0.568$. Pressure side (**left**) and suction side (**right**).

For the Reynolds number $\mathrm{Re} = 5 \times 10^5$, the numerical results are also compared with two sets of experiments carried out at MARIN with and without leading-edge roughness (LER). For the tests with LER the entire leading-edge was roughened with 60 µm carborundum grains. The paint-test photos published in Boorsma [49] are shown in Figure 17, where laminar and turbulent flow regimes are visualised over the propeller blades. On the inner radii until $r/R = 0.5$ of the smooth propeller, laminar flow is seen until approximately 70% of the blade chord, followed by transition to turbulent flow on the pressure side and trailing-edge separation on the suction side. On the outer radii, transition occurs before the blade mid-chord. On the propeller with LER, the roughness becomes effective around $r/R = 0.5$ and turbulent flow develops from the leading-edge.

Since surface roughness is used to force the flow to the turbulent regime, the numerical results obtained with the $k-\omega$ SST turbulence model are compared with the paint-test from the propeller with LER. From the examination of the paint-test photos and limiting streamlines, different flow patterns are obtained at the inner radii. At the outer radii, the $k-\omega$ SST turbulence model predicts transition near the leading-edge on both sides of the propeller blade bringing the limiting streamlines to a good agreement with the streamline patterns. For the smooth propeller experiments, where natural transition is expected to occur, the numerical results obtained with the $\gamma - \tilde{\mathrm{Re}}_{\theta_t}$ transition model are compared with the paint-tests. However, due to the limitations of the $\gamma - \tilde{\mathrm{Re}}_{\theta_t}$ transition model for blind prediction of transitional flow, the inlet turbulence quantities were selected in a previous study, see Baltazar et al. [24], in order to have a good agreement between the limiting streamlines and the paint-tests.

For the lower Reynolds numbers, a laminar flow regime is predicted by both models, since the limiting streamlines are more radially directed. With the increase in the Reynolds number the limiting streamlines become more circumferentially directed and the separation region near the trailing-edge reduces from the higher to the lower radii. Significant

differences are seen in the blade boundary-layer flow predicted by the $k-\omega$ SST turbulence model and $\gamma-\tilde{\mathrm{Re}}_{\theta_t}$ transition model for the Reynolds numbers between 1×10^5 and 1×10^6. At these flow regimes, transition from laminar to turbulent flow occurs earlier with the $k-\omega$ SST turbulence model. For the higher Reynolds number, a turbulent flow regime over the blade surface is predicted by both models. Still, a small laminar flow region near the blade leading-edge is obtained with the $\gamma-\tilde{\mathrm{Re}}_{\theta_t}$ transition model.

In order to understand the differences in the flow solutions between the $k-\omega$ SST turbulence model and the $\gamma-\tilde{\mathrm{Re}}_{\theta_t}$ transition model, the pressure and skin friction distributions at the radial section 0.7 are presented in Figure 20. The non-dimensional chordwise coordinate is defined as s/c. Similar pressure distributions are obtained with the turbulence and transition models, with the exception for the Reynolds number $\mathrm{Re}=1\times10^5$, where different separated regions are predicted along the blade trailing-edge. For the skin friction coefficient, distinct distributions and transition locations are obtained with the turbulence and transition models. These results show that RANS models can be used not only to estimate the propeller forces at different scales, but provide also detailed information of the boundary-layer flow over the blade.

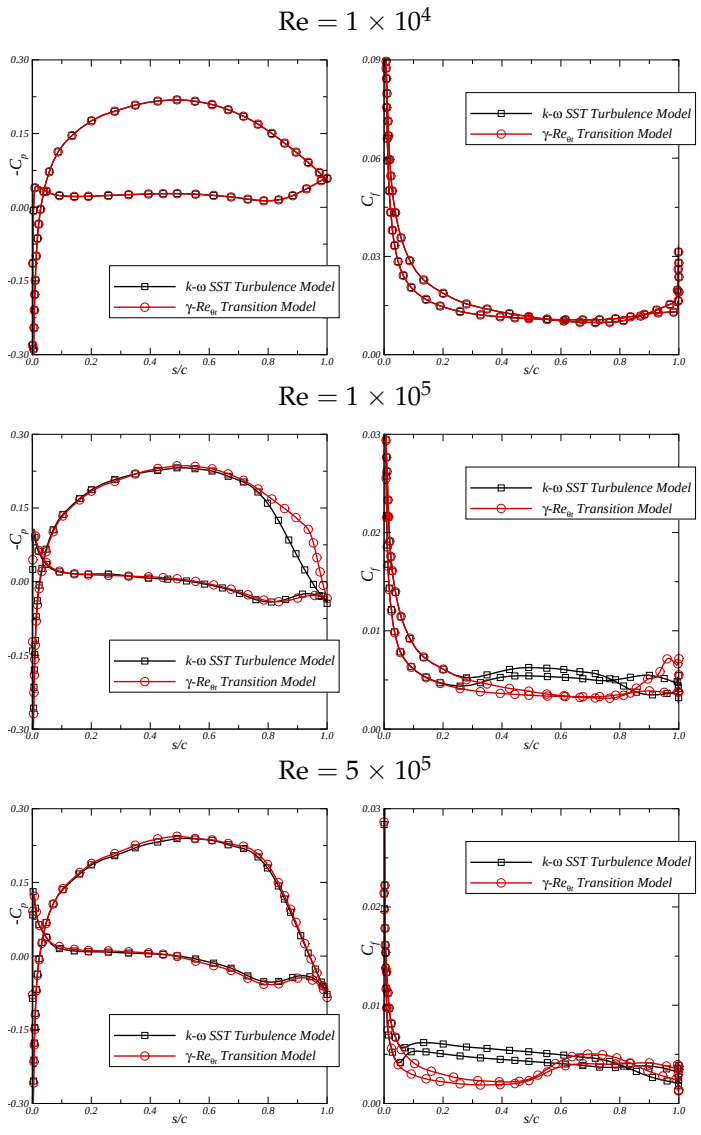

Figure 20. *Cont.*

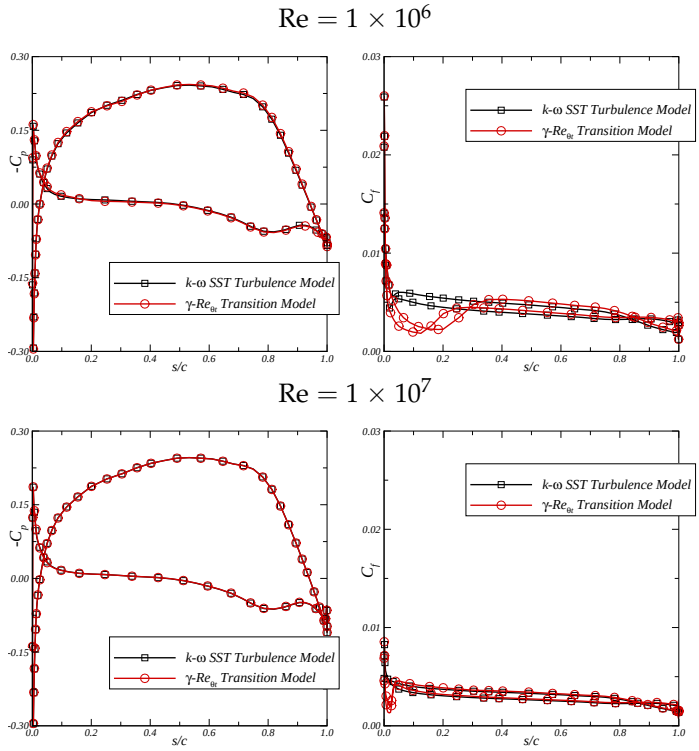

Figure 20. Blade pressure C_p (**left**) and skin friction C_f (**right**) distributions at $r/R = 0.7$ with the $k-\omega$ SST turbulence model and $\gamma - \tilde{\mathrm{Re}}_{\theta_t}$ transition model.

In addition to pressure and skin friction coefficients, the blade boundary-layer flow can be analysed from the evolution of the boundary-layer thickness δ, displacement thickness δ^* and shape factor H at the different Reynolds numbers. The boundary-layer characteristics are shown in Figures 21 and 22. The estimated boundary-layer thickness is obtained from the total pressure loss Δp_t:

$$\Delta p_t = P + \frac{1}{2}\rho\left[V_x^2 + V_y^2 + V_z^2\right] - P_{\text{inlet}} - \frac{1}{2}\rho\left[U^2 + (\Omega r)^2\right], \tag{17}$$

where $P_{\text{inlet}} = p_\infty + 2/3\rho k_{\text{inlet}}$. The boundary-layer thickness is defined by the distance normal from the blade surface to a point where the total pressure loss coefficient $C_{\Delta p_t} = \Delta p_t/(1/2\rho V_{\text{ref}}^2)$ is equal to -0.01. The boundary-layer thickness reduces with the increase in Reynolds number, where a much thicker boundary-layer is observed for the lower Reynolds number. Furthermore and associated with the adverse pressure gradient, a thicker boundary-layer is observed on the suction side in comparison with the pressure side. A similar behaviour is obtained for the displacement thickness. As expected, a distinction between laminar and turbulent flow regimes is visible in the boundary-layer parameters. The transition in the flow regime is especially marked in the drop of the shape factor.

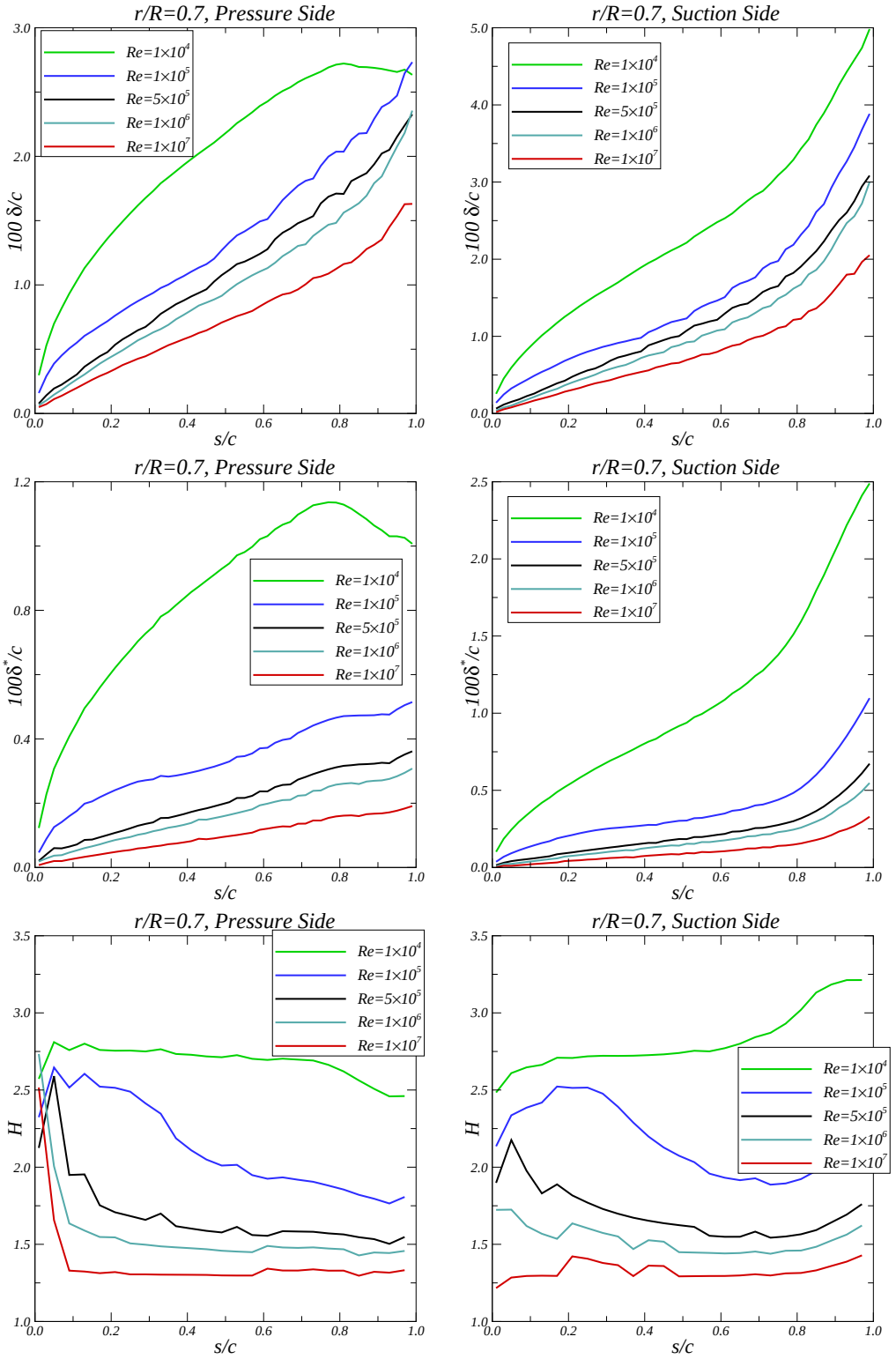

Figure 21. Boundary-layer thickness δ (**top**), displacement thickness δ^* (**middle**), and shape factor H (**bottom**) at $r/R = 0.7$ using the $k-\omega$ SST turbulence model.

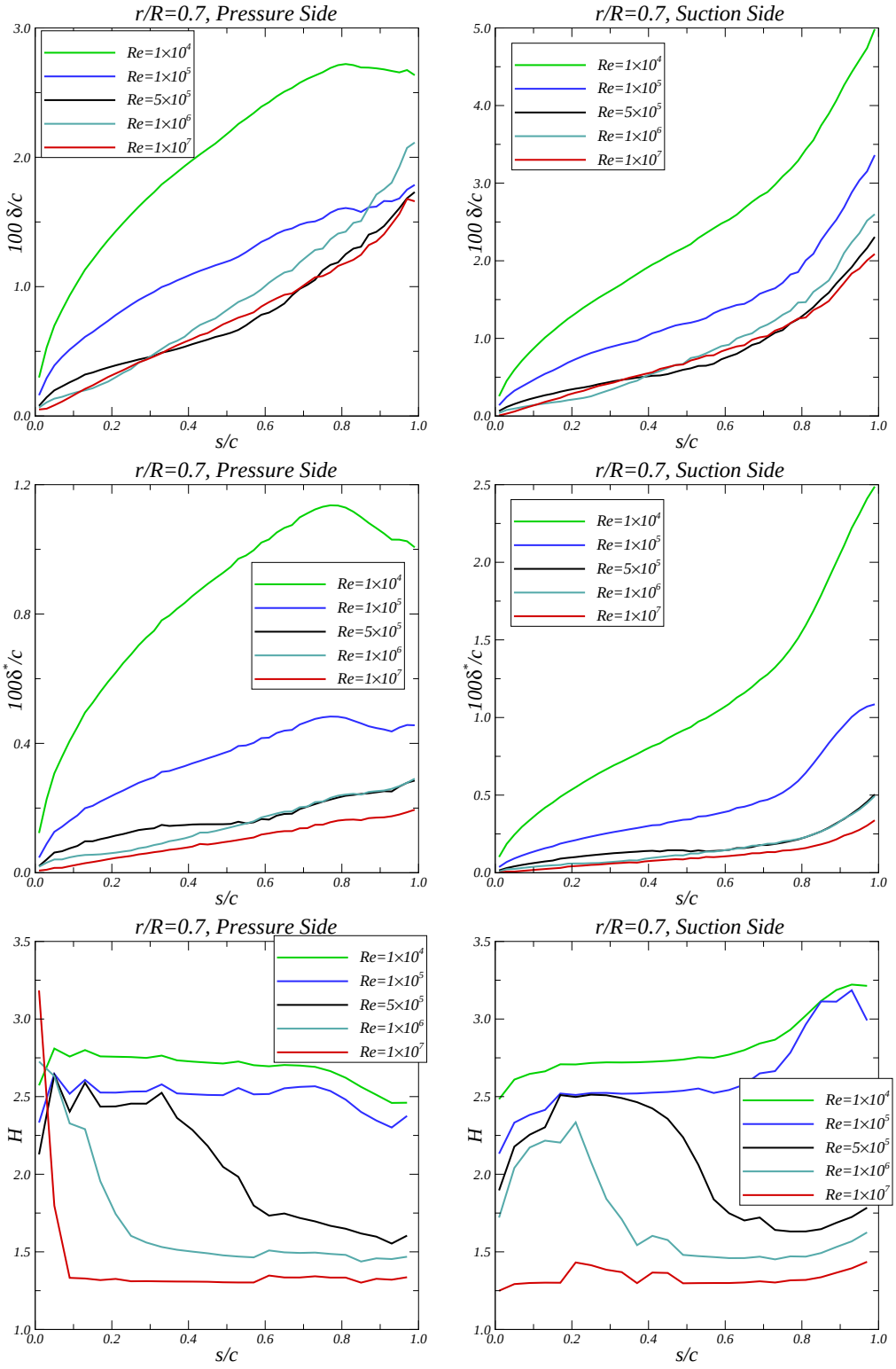

Figure 22. Boundary-layer thickness δ (**top**), displacement thickness δ^* (**middle**), and shape factor H (**bottom**) at $r/R = 0.7$ using the $\gamma - \tilde{\mathrm{Re}}_{\theta_t}$ transition model.

5. Performance Prediction

In this section the influence of the Reynolds number on the predicted propulsive performance is investigated. Table 8 presents the propeller thrust and torque coefficients for the various Reynolds numbers, including the pressure and friction contributions, obtained with the $k - \omega$ SST turbulence model and $\gamma - \tilde{\mathrm{Re}}_{\theta_t}$ transition model, respectively. The pre-

diction of the scale-effects on the propeller thrust and torque compared to Re $= 5 \times 10^5$ is also included. The evolution of the propeller performance characteristics with the Reynolds number is also shown in Figure 23.

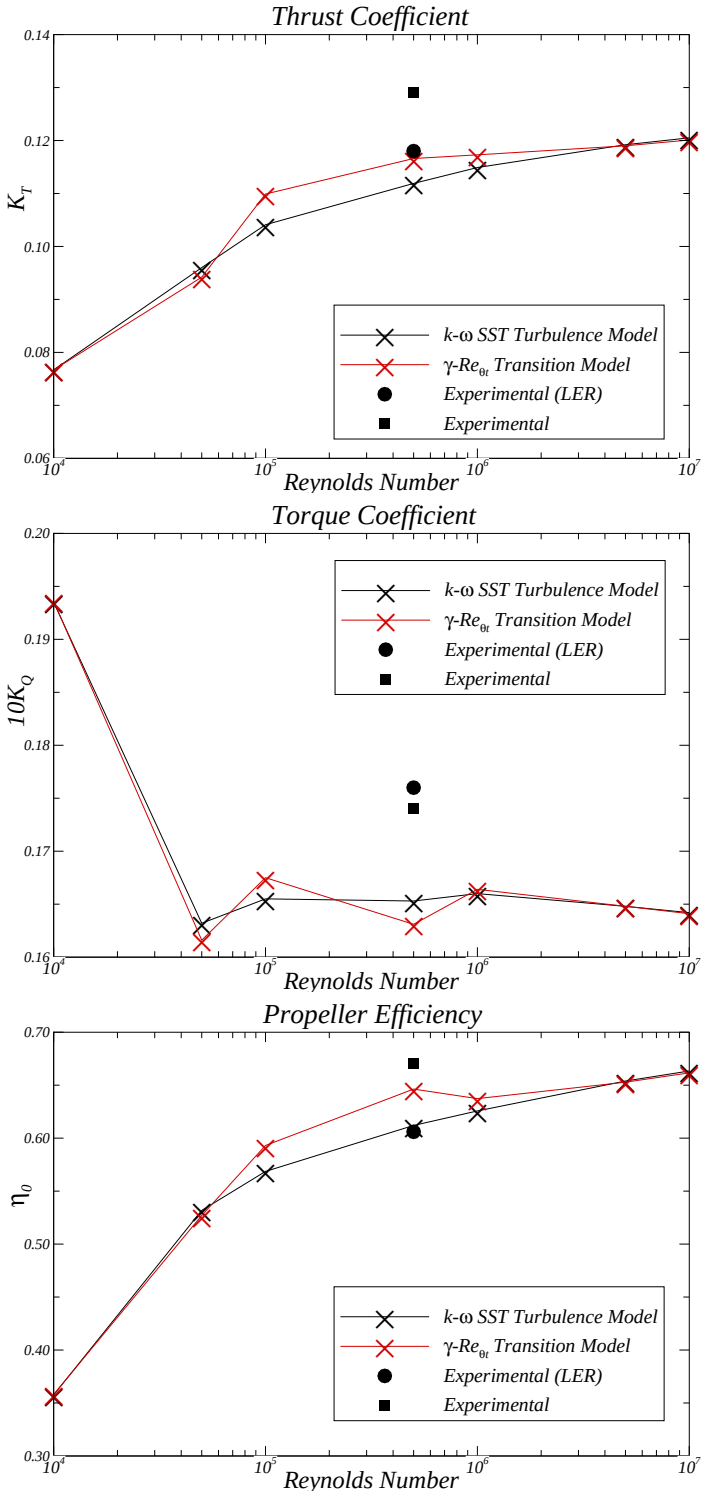

Figure 23. Propeller performance prediction for different Reynolds numbers at $J = 0.568$ using the $k - \omega$ SST turbulence model and the $\gamma - \tilde{\mathrm{Re}}_{\theta_t}$ transition model.

From the results, an increase in the propeller thrust with the rising of the Reynolds number is obtained for both models. For the torque coefficient, with the exception of the lower Reynolds number (Re $= 1 \times 10^4$), small variations are found. In addition, with the

increase of the Reynolds number a growth in the pressure contribution to the propeller force coefficients is observed. For the friction contribution, a decrease is obtained with the rising of the Reynolds number. However, an oscillatory behaviour is observed at $\mathrm{Re} = 1 \times 10^5$ for the $\gamma - \tilde{\mathrm{Re}}_{\theta_t}$ transition model. For the full-scale Reynolds number ($\mathrm{Re} = 1 \times 10^7$), an increase in the propeller thrust of 7.7% with the $k - \omega$ SST turbulence model and of 3% with the $\gamma - \tilde{\mathrm{Re}}_{\theta_t}$ transition model compared to model-scale ($\mathrm{Re} = 5 \times 10^5$) are obtained. For the propeller torque, small variations are observed, with 0.7% reduction for the $k - \omega$ SST turbulence model and 0.6% increase for the $\gamma - \tilde{\mathrm{Re}}_{\theta_t}$ transition model. We note that these differences are smaller than the estimated numerical uncertainty.

Table 8. Pressure ($_p$) and friction ($_f$) contributions to the propeller thrust and torque coefficients at $J = 0.568$. Prediction of the scale-effects on K_T compared to $\mathrm{Re} = 5 \times 10^5$.

Re	K_{T_p}	K_{T_f}	K_T	ΔK_T	$10K_{Q_p}$	$10K_{Q_f}$	$10K_Q$	ΔK_Q
				$k - \omega$ SST				
1×10^4	0.0839	−0.00722	0.0767	−31.5%	0.1164	0.0772	0.1935	17.1%
5×10^4	0.0992	−0.00323	0.0960	−14.2%	0.1274	0.0357	0.1632	−1.3%
1×10^5	0.1070	−0.00290	0.1041	−7.0%	0.1330	0.0325	0.1655	0.1%
5×10^5	0.1143	−0.00242	0.1119	–	0.1394	0.0260	0.1653	–
1×10^6	0.1171	−0.00219	0.1149	2.7%	0.1428	0.0232	0.1660	0.4%
5×10^6	0.1209	−0.00172	0.1192	6.5%	0.1468	0.0180	0.1648	−0.3%
1×10^7	0.1221	−0.00154	0.1205	7.7%	0.1481	0.0161	0.1642	−0.7%
				$\gamma - \tilde{\mathrm{Re}}_{\theta_t}$				
1×10^4	0.0839	−0.00722	0.0767	−34.2%	0.1164	0.0772	0.1936	18.7%
5×10^4	0.0974	−0.00314	0.0942	−19.2%	0.1272	0.0344	0.1616	−0.9%
1×10^5	0.1120	−0.00215	0.1099	−5.7%	0.1435	0.0240	0.1675	2.7%
5×10^5	0.1183	−0.00172	0.1166	–	0.1439	0.0192	0.1631	–
1×10^6	0.1193	−0.00196	0.1173	0.6%	0.1453	0.0211	0.1664	2.0%
5×10^6	0.1207	−0.00174	0.1190	2.1%	0.1466	0.0181	0.1648	1.0%
1×10^7	0.1217	−0.00158	0.1201	3.0%	0.1477	0.0164	0.1641	0.6%

The different estimations of the scale-effects are influenced by the distinct propeller flow simulations obtained by the $k - \omega$ SST turbulence model and $\gamma - \tilde{\mathrm{Re}}_{\theta_t}$ transition model at model-scale ($\mathrm{Re} = 5 \times 10^5$). The propeller force predictions at $\mathrm{Re} = 5 \times 10^5$ are compared with the experiments in Table 9. A higher thrust coefficient is obtained with the $\gamma - \tilde{\mathrm{Re}}_{\theta_t}$ transition model, similar to the experimental measurements for the smooth propeller. The relative differences for the thrust coefficient are equal to −9.6% for the $\gamma - \tilde{\mathrm{Re}}_{\theta_t}$ transition model in comparison with the smooth propeller, and −5.2% for the $k - \omega$ SST turbulence model in comparison to the propeller with LER. For the propeller torque, a minor effect due to the application of LER is seen in the experimental measurements. A similar effect is observed in the numerical predictions from both models. The relative differences for the torque coefficient are in the order of 6%.

Table 9. Propeller force predictions at $\mathrm{Re} = 5 \times 10^5$ for $J = 0.568$. Comparison with experimental results [49].

	K_T	$10K_Q$
$k - \omega$ SST	0.1119	0.1653
$\gamma - \tilde{\mathrm{Re}}_{\theta_t}$	0.1166	0.1631
Experimental (LER)	0.118	0.176
Experimental	0.129	0.174

6. Conclusions

In this paper viscous flow calculations using a RANS code are presented for a marine propeller in open-water conditions at different Reynolds numbers ranging from 10^4 to 10^7. The $\gamma - \tilde{\mathrm{Re}}_{\theta_t}$ transition model, which solves two additional equations, γ and $\tilde{\mathrm{Re}}_{\theta_t}$, for predicting flow transition is considered and results are compared to the commonly used $k - \omega$ SST turbulence model, where flow transition is taken care implicitly by the model. The results presented in this study can be summarised as follows:

- For the various Reynolds number calculations and due to the strong dependence of the $\gamma - \tilde{\mathrm{Re}}_{\theta_t}$ transition model on the inlet turbulence quantities, a relation between the inlet eddy-viscosity ratio and the Reynolds number has been found to maintain the decay rate of the turbulence quantities along the streamwise direction. On the contrary, a minor effect to the inlet turbulence quantities is obtained with the $k - \omega$ SST turbulence model.
- The influence of the iterative error and discretisation error in the propeller force predictions has been studied. Results show that convergence of the intermittency γ is not obtained for the higher Reynolds numbers. Still, a negligible effect is expected on the predicted propeller forces, since global convergence is achieved for the momentum and continuity equations in all cases. The discretisation error was estimated from a procedure based on grid refinement studies. In this analysis an apparent order of convergence between 1 and 2 is observed, and the predicted numerical uncertainties are in the order of 0.4–4.2%.
- A detailed analysis of the blade boundary-layer flow was made. Different flow solutions are obtained with the $k - \omega$ SST turbulence model and $\gamma - \tilde{\mathrm{Re}}_{\theta_t}$ transition model in the range between $\mathrm{Re} = 1 \times 10^5$ and 1×10^6. At these Reynolds numbers, transition from laminar to turbulent flow occurs earlier with the $k - \omega$ SST turbulence model. As expected, a laminar flow regime is predicted by both models for lower Reynolds numbers, whereas a turbulent flow regime is obtained for higher Reynolds numbers.
- At model-scale Reynolds number ($\mathrm{Re} = 5 \times 10^5$), the limiting streamlines have been compared with paint flow tests for the propeller with and without LER. The limiting streamlines produced by the $k - \omega$ SST turbulence model agree well on the outer part of the rough propeller. For the smooth propeller, the inlet turbulence quantities of the $\gamma - \tilde{\mathrm{Re}}_{\theta_t}$ transition model were selected to match the paint-tests.
- The propulsive predictions obtained by the $k - \omega$ SST turbulence model and $\gamma - \tilde{\mathrm{Re}}_{\theta_t}$ transition model near the design operating point show an increase in the thrust coefficient for rising Reynolds number. For the torque coefficient, with the exception of the lower Reynolds number ($\mathrm{Re} = 1 \times 10^4$), small variations are achieved. These variations result in an increase of the open-water efficiency between model- and full-scale. Compared to the model-scale Reynolds number ($\mathrm{Re} = 5 \times 10^5$), an increase in the thrust coefficient of 7.7% and 3.0% is obtained with the $k - \omega$ SST turbulence model and $\gamma - \tilde{\mathrm{Re}}_{\theta_t}$ transition model, respectively.

Results show that flow transition should be taken into account in the RANS simulations for more accurate predictions of the scale-effects on propellers. Transition models offer an opportunity to investigate and compare the propeller flow at different scales. However, the strong sensitivity of the $\gamma - \tilde{\mathrm{Re}}_{\theta_t}$ transition model to the inlet turbulence quantities inhibits its use for blind comparisons. Two difficulties have been identified from this study: more accurate predictions require correct information of the turbulence intensity and eddy-viscosity (or turbulence dissipation rate) for the specification of the inlet turbulence quantities which is seldom available; the nonphysical strong decay of the turbulence intensity that is predicted by the turbulence model. In this study the boundary conditions for the turbulence quantities have been calibrated from experimental paint-tests at one Reynolds number to match qualitatively the transition location. The decay of the turbulence intensity from the inlet to the propeller region was controlled by specifying unreasonable large eddy-viscosity ratios.

Author Contributions: J.B. conducted the viscous calculations with the RANS solver and analysed the numerical results. D.R. generated the grids and participated in the development of the RANS code ReFRESCO. J.F.d.C. provided scientific advice and supervision throughout. All authors discussed the results and commented on the manuscript. All authors have read and agreed to the published version of the manuscript.

Funding: The work was also supported by FCT/MCTES (PIDDAC) through project LARSyS—FCT Pluriannual funding 2020–2023 (UIDB/EEA/50009/2020).

Acknowledgments: The authors acknowledge the Laboratory for Advanced Computing at University of Coimbra for providing computing resources that have contributed to part of the research results reported within this paper. URL: https://www.uc.pt/lca (accessed on 13 October 2021).

Conflicts of Interest: The authors declare no conflict of interest.

Abbreviations

The following abbreviations are used in this manuscript:

CFD	Computational Fluid Dynamics
FCT	Fundação para a Ciência e Tecnologia
ITTC	International Towing Tank Conference
LARSys	Laboratory for Robotics and Engineering Systems
LER	Leading-edge roughness
MARETEC	Marine, Environment and Technology Centre
MARIN	Maritime Research Institute Netherlands
MCTES	Ministério da Ciência, Tecnologia e Ensino Superior
PIDDAC	Programa de Investimentos e Despesas de Desenvolvimento da Administração Central
QUICK	Quadratic upwind interpolation for convective kinematics
RANS	Reynolds-averaged Navier-Stokes
SIMPLE	Semi-implicit method for pressure linked equations
SST	Shear-stress transport

References

1. ITTC. 1978 ITTC Performance Prediction Method. Section 7.5-02-03-01.4. In Proceedings of the 28th International Towing Tank Conference, Wuxi, China, 18–22 September 2017.
2. ITTC Propulsion Committee. Final Report and Recommendations to the 27th ITTC. In Proceedings of the 27th International Towing Tank Conference, Copenhagen, Denmark, 31 August–5 September 2014.
3. ITTC Propulsion Committee. Final Report and Recommendations to the 28th ITTC. In Proceedings of the 28th International Towing Tank Conference, Wuxi, China, 18–22 September 2017.
4. Meyne, K. Untersuchung der Propellergrenzschichtströmung und der Einfluss der Reibung auf die Propellerkenngrössen (Investigation of Propeller Boundary-Layer Flow and Friction Effects on Propeller Characteristics). In *Jahrbuch der Schiffbautechnischen Gesellschaft*; Band 66; Also DTNSRDC Translation 352; Springer: Berlin, Germany, 1972.
5. Kuiper, G. Scale Effects on Propeller Cavitation Inception. In Proceedings of the 12th ONR Symposium on Naval Hydrodynamics, Washington, DC, USA, 5–9 June 1978.
6. Kuiper, G. Cavitation Inception on Ship Propeller Models. Ph.D. Thesis, Delft University of Technology, The Netherlands, 1981.
7. Driver, D. Application of oil-film interferometry skin-friction measurement to large wind tunnels. *Exp. Fluids* **2003** *34*, 717–725.
8. Schülein, E.; Rosemanny, H.; Schaber, S. Transition detection and skin friction measurements on rotating propeller blades. In Proceedings of the 28th Aerodynamic Measurement Technology, Ground Testing, and Flight Testing Conference, New Orleans, LA, USA, 25–28 June 2012.
9. Wolf, C.; Gardner, A; Raffel, M. Infrared thermography for boundary layer transition measurements. *Meas. Sci. Technol.* **2020** *31*, 112002.
10. Stanier, M. The Application of RANS Code to Investigate Propeller Scale Effects. In Proceedings of the 22th ONR Symposium on Naval Hydrodynamics, Washington, DC, USA, 9–14 August 1998.
11. Funeno, I. On viscous flow around marine propellers. *J. Kansai Soc. Nav. Arch. Jpn.* **2002**, *238*, 17–27.
12. Krasilnikov, V.; Sun, J.; Halse, K. CFD Investigation in Scale Effects on Propellers with Different Magnitude of Skew in Turbulent Flow. In Proceedings of the First International Symposium on Marine Propulsors, Trondheim, Norway, 22–24 June 2009.
13. Sánchez-Caja, A.; González-Adalid, J.; Pérez-Sobrino, M.; Sipilä, T. Scale effects on tip loaded propeller performance using a RANSE solver. *Ocean Eng.* **2014**, *88*, 607–617.
14. Rijpkema, D.; Baltazar, J.; Falcão de Campos, J. Viscous Flow Simulations of Propellers in Different Reynolds Number Regimes. In Proceedings of the Fourth International Symposium on Marine Propulsors, Austin, TX, USA, 31 May–4 June 2015.

15. Abdel-Maksoud, M.; Heinke, H.-J. Scale Effects on Ducted Propellers. In Proceedings of the 24th ONR Symposium on Naval Hydrodynamics, Fukuoka, Japan, 8–13 July 2002.
16. Haimov, H.; Vicario, J.; del Corral, J. RANSE Code Application for Ducted and Endplate Propellers in Open Water. In Proceedings of the Second International Symposium on Marine Propulsors, Hamburg, Germany, 15–17 June 2011.
17. Rijpkema, D.; Vaz, G. Viscous Flow Computations on Propulsors: Verification, Validation and Scale Effects. In Proceedings of the International Conference on Developments in Marine CFD, London, UK, 22–23 March 2011.
18. Langtry, R. A Correlation-Based Transition Model Using Local Variables for Unstructured Parallelized CFD Codes. Ph.D. Thesis, University of Stuttgart, Stuttgart, Germany, 2006.
19. Langtry, R.; Menter, F. Correlation-based transition modeling for unstructured parallelized computational fluid dynamics codes. *AIAA J.* **2009**, *47*, 2894–2906.
20. Walters, D.; Cokljat, D. A three-equation eddy-viscosity model for Reynolds-averaged Navier-Stokes simulations of transitional flow. *ASME J. Fluids Eng.* **2008**, *130*, 121401.1–121401.14.
21. Müller, S.-B.; Abdel-Maksoud, M.; Hilbert, G. Scale Effects on Propellers for Large Container Vessels. In Proceedings of the First International Symposium on Marine Propulsors, Trondheim, Norway, 22–24 June 2009.
22. Eça, L.; Lopes, R.; Vaz, G.; Baltazar, J.; Rijpkema, D. Validation Exercises of Mathematical Models for the Prediction of Transitional Flows. In Proceedings of the 31st Symposium on Naval Hydrodynamics, Monterey, CA, USA, 11–16 September 2016.
23. Yao, H.; Zhang, H. A simple method for estimating transition locations on blade surface of model propellers to be used for calculating viscous force. *Int. J. Nav. Archit. Ocean Eng.* **2018**, *10*, 477–490.
24. Baltazar, J.; Rijpkema, D.; Falcão de Campos, J.A.C. On the use of the $\gamma - \tilde{\mathrm{Re}}_{\theta_t}$ transition model for the prediction of the propeller performance at model-scale. *Ocean Eng.* **2018**, *170*, 6–19.
25. Gaggero, S. Influence of laminar-to-turbulent transition on model scale propeller performances. Part I: Fully wetted conditions. *Ship Offshore Struct.* **2020**, doi:10.1080/17445302.2020.1863658.
26. Bhattacharyya, A.; Krasilnikov, V.; Steen, S. Scale effects on open water characteristics of a controllable pitch propeller working within different duct designs. *Ocean Eng.* **2016**, *112*, 226–242.
27. Pawar, S.; Brizzolara, S. Relevance of transition turbulent model for hydrodynamic characteristics of low Reynolds number propeller. *Appl. Ocean Res.* **2019**, *87*, 165–178.
28. Krasilnikov, V.; Sileo, L.; Steinsvik, K. Numerical Investigation into Scale Effect on the Performance Characteristics of Twin-Screw Offshore Vessels. In Proceedings of the Fifth International Symposium on Marine Propulsors, Espoo, Finland, 12–15 June 2017.
29. Moran-Guerrero, A.; Gonzalez-Gutierrez, L.M.; Oliva-Remola, A.; Diaz-Ojeda, H.R. On the influence of transition modeling and crossflow effects on open water propeller simulations. *Ocean Eng* **2018**, *156*, 101–119.
30. Viitanen, V.; Siikonen, T.; Sánchez-Caja, A. Cavitation on model- and full-scale marine propellers: Steady and transient viscous flow simulations at different Reynolds numbers. *J. Mar. Sci. Eng.* **2020**, *8*, 141.
31. Gaggero, S. Influence of laminar-to-turbulent transition on model scale propeller performances. Part II: Cavitating conditions. *Ship Offshore Struct.* **2020**, doi:10.1080/17445302.2020.1866819.
32. Schnerr, G.; Sauer, J. Physical and Numerical Modeling of Unsteady Cavitation Dynamics. In Proceedings of the 4th International Conference on Multiphase Flow, New Orleans, LA, USA, 27 May–1 June 2001.
33. Wang, X.; Walters, K. Computational analysis of marine-propeller performance using transition-sensitive turbulence modeling. *ASME J. Fluids Eng.* **2012**, *134*, 071107.1–071107.10.
34. Gaggero, S.; Villa, D. Improving model scale propeller performance prediction using the $k - k_L - \omega$ transition model in OpenFOAM. *Int. Ship Prog.* **2018**, *65*, 187–226.
35. Lopes, R.; Eça, L.; Vaz, G. On the numerical behavior of RANS-based transition models. *ASME J. Fluids Eng.* **2020**, *142*, 051503.1–051503.14.
36. Menter, F. Two-equation eddy viscosity turbulence models for engineering applications. *AIAA J.* **1994**, *32*, 1598–1605.
37. Menter, F.; Kuntz, M.; Langtry, R. Ten Years of Industrial Experience with the SST Turbulence Model. In Proceedings of the Fourth International Symposium on Turbulence, Heat and Mass Transfer, Antalya, Turkey, 12–17 October 2003.
38. Eça, L.; Hoekstra, M. The numerical friction line. *J. Mar. Sci. Technol. 2008*, *13*, 328–345.
39. Wilcox, D. Reassessment of the scale-determining equation for advanced turbulence models. *AIAA J.* **1988**, *26*, 1299–1310.
40. Baltazar, J.; Melo, D.; Rijpkema, D. Analysis of the blade boundary-layer flow of a marine propeller using a RANS solver. *Ocean Eng.* **2020**, *211*, 107633.
41. Schmitt, F. About Boussinesq's turbulent viscosity hypothesis: Historical remarks and a direct evaluation of its validity. *C. R. Méc.* **2007**, *335*, 617–627.
42. Jones, W.; Launder, B. The prediction of laminarization with a two-equation model of turbulence. *Int. J. Heat Mass Transf.* **1972**, *15*, 301–314.
43. Langtry, R.B.; Sengupta, K.; Yeh, D.T.; Dorgan, A.J. Extending the $\gamma - Re_{\theta t}$ Local Correlation based Transition Model for Crossflow Effects. In Proceedings of the 45th AIAA Fluid Dynamics Conference, Dallas, TX, USA, 22–26 June 2015; AIAA 2015-2474.
44. Grabe, C.; Shengyang, N.; Krumbein, A. Transition Transport Modeling for the Prediction of Crossflow Transition. In Proceedings of the 34th AIAA Applied Aerodynamics Conference, Washington, DC, USA, 13–17 June 2016; AIAA2016-3572.
45. Grabe, C.; Shengyang, N.; Krumbein, A. Transport modeling for the prediction of crossflow transition. *AIAA J.* **2018**, *56*, 3167–3178.
46. Spalart, P.; Rumsey, C. Effective inflow conditions for turbulence models in aerodynamic calculations. *AIAA J.* **2007**, *45*, 2544–2553.

47. Vaz, G.; Jaouen, F.; and Hoekstra, M. Free-Surface Viscous Flow Computations: Validation of URANS Code FreSCo. In Proceedings of the ASME 2009 28th International Conference on Ocean, Offshore and Arctic Engineering, Honolulu, HI, USA, 31 May–5 June 2009.
48. Jonk, A.; Willemsen, H. *Calm Water Model Tests for a 300,000 DWT Crude Oil Carrier*; Tech. Rep. 012383-1-VT; MARIN: Wageningen, The Netherlands, 1994.
49. Boorsma, A. Improving Full Scale Ship Powering Performance Predictions by Application of Propeller Leading Edge Roughness. Part 1: Effect of Leading Edge Roughness on Propeller Performance. Master's Thesis, Delft University of Technology, Delft, The Netherlands, 2000.
50. GridPro. Available online: http://www.gridpro.com (accessed on 17 June 2021).
51. Oberkampf, W.; Roy, C. *Verification and Validation in Scientific Computing*; Cambridge University Press: New York, NY, USA, 2010.
52. Eça, L.; Hoekstra, M. A Procedure for the Estimation of the Numerical Uncertainty of CFD Calculations Based on Grid Refinement Studies. *J. Comput. Phys.* **2014**, *262*, 104–130.